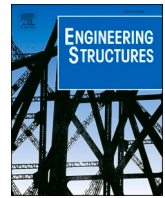




Contents lists available at ScienceDirect

Engineering Structures

journal homepage: www.elsevier.com/locate/engstruct

Limit-state analysis of parabolic arches subjected to inertial loading in different gravitational fields using a variational formulation

G. Kampas^{a,*}, N. Kalapodis^a, T. McLean^b, C. Málaga-Chuquitaype^b

^a School of Engineering, University of Greenwich, UK

^b Department of Civil and Environmental Engineering, Imperial College London, UK

ARTICLE INFO

Keywords:

Seismic analysis
Low-gravity conditions
Minimum thickness
Failure mechanism
Extraterrestrial structures

ABSTRACT

For thousands of years, arches have been used as durable structures that are easy to build and that rely on gravity for their inherent stability. Since then, many researchers and engineers have studied their stability either when subjected to gravity or inertial loading. Currently, given the Insight mission to Mars and the ambitious Artemis program to the Moon, it has become apparent that there will soon be the need to design and build the first resilient extraterrestrial structures and arches represent an ideal option for such structures. This paper focuses on the stability of parabolic arches with different embrace angles subjected to different levels of equivalent inertial loading in low-gravity conditions. The results are contrasted with the well-studied circular arches. More specifically, this investigation employs variational principles to identify the imminent mechanisms and numerical methods based on the limit thrust line concept in order to estimate the minimum required thickness of parabolic arches for a given loading and in different gravitational fields. The paper shows that although parabolic arches can be much more efficient than their circular counterparts for gravitational-only loading, this is not the case for different combinations of inertial loading and embrace angles where the opposite can be true. It highlights the dominant effect of low-gravity conditions on the minimum thickness requirements for both types of arches and considers the effect of a potential additional infill for radiation shielding. Furthermore, this study reveals a self-similar behaviour, introduces a “universal” inertial loading and showcases, through the use of master curves, the areas where the parabolic arches are more efficient than their circular counterparts and those where the opposite is true. These areas can be used for the preliminary design of such structures. Additionally, the paper identifies hidden patterns associated with the developed mechanisms between the two different geometries for the different gravitational fields. Finally, it presents a case study where the need to optimise the structural form of extraterrestrial structures becomes evident.

1. Introduction

Nowadays, following the new space era towards the exploration and potential human settlement in other planetary bodies, various space agencies (NASA, ESA, ISRO, etc) and private firms (SpaceX, Virgin Galactic, Blue Origin, etc) are investing in ambitious missions such as “Artemis” amongst others. Hence, it is only a matter of time before designing and building the first extraterrestrial habitats [43], initially on the Moon and later on Mars. There have been many concepts and ideas proposed in the past, as summarised by Kalapodis et al. [24], but the most prevalent is the need for an external resilient shielding structure that would protect valuable assets (energy fuel tanks, robotic elements, future inflatable modules, etc) from extreme radiation [38] and

temperature fluctuations [5,23]. These structures can be made from local soil called regolith [12,44] in line with the In-Situ Resource Utilisation (ISRU) framework [37], as shown in Fig. 1a. This is proposed to be an arch-like structure in order to: (a) span large distances as a potential storage facility and (b) act mainly in compression since regolith is not expected to exhibit significant tensile strength as a structural material [8], while it will be able to provide the necessary compressive strength [9,18]. At the same time, this structure will need to be resilient against strong ground motions generated by shallow moonquakes [31,34] and marsquakes with epicentres close to the structure or generated by meteoroid impacts [14,13].

Arches are curved structural forms that have proven to be very resilient and durable as structures since ancient Egypt with the famous

* Corresponding author.

E-mail address: G.Kampas@gre.ac.uk (G. Kampas).

<https://doi.org/10.1016/j.engstruct.2020.111501>

Received 2 June 2020; Received in revised form 21 October 2020; Accepted 27 October 2020

0141-0296/© 2020 The Authors. Published by Elsevier Ltd. This is an open access article under the CC BY license (<http://creativecommons.org/licenses/by/4.0/>).

adobe Ramesseum vaults in 1250BC [15], ancient Greece with masonry vaults as entrances to stadiums (Olympia, Nemea) and ancient Rome with masonry bridges and aqueducts as shown in Fig. 1 b,c. The common advantage between these structures is that their stability depends mainly on compression and therefore gravity. Some widely-adopted assumptions for masonry arches are: (a) that they act as rigid, (b) they have infinite compressive strength and (c) zero tensile strength ([12,36,10,30,22,30;1–3] amongst others), and thus can be analysed by utilising a well-known concept: the thrust-line. Furthermore, the use of the funicular polygon from thrust line analysis can reveal important aspects about the effect of the shear force on masonry structures with voissiors.

Different types of arch geometries have been adopted throughout the centuries depending on many parameters such as aesthetics, function, target span, and the structural material utilised. The most common configurations are circular, elliptical, parabolic, catenary and pointed arches. A distinct advantage of parabolic arches is that they can span large distances given the appropriate set of parameters and hence, constitute a common practice in bridge design amongst other applications. However, such arches develop high amounts of thrust at the springing [4]. Yet, there is no extensive literature on finite-thickness parabolic arches, especially focussing on limit-state analysis [39].

Some of the greatest engineers and scientists of modern history have studied the stability of arches. Hooke [20] was the first to introduce the inverted chain concept through his famous anagram “*as hangs the flexible line, so but inverted will stand the rigid arch*” describing the catenary shape (alysoid). However, it was Couplet [11] who studied first the minimum thickness of semicircular arches with finite thickness (two-dimensional) under their self-weight. It was Milankovitch [30] that expressed the semicircular arch in polar coordinates and managed to estimate the exact locations of the “intrados” hinges at 54.48° from the crown of the arch, the minimum thickness of the arch as 0.1075 of the centreline radius, and that the catenary is not an admissible thrust line, by providing an analytical expression for the thrust line. These results were later confirmed by Makris and Alexakis [27] who discovered that not only is the catenary not an admissible thrust line, but that the arch’s stereotomy affects the shape of its thrust line and minimum thickness. Subsequently, Alexakis and Makris [1] investigated the minimum thickness of elliptical arches subjected to their self-weight and arrived to similar results; that the thrust line depends on the stereotomy and on the aspect ratio (rise over span) of the elliptical shape. Furthermore, they progressed with identifying the minimum thickness of semicircular arches when subjected to horizontal accelerations leading to four-hinge failure mechanisms [3], building on Clemente’s [9] and Oschendorf’s [35] pioneering work.

In light of the above, this paper presents the results from the limit-state analysis of parabolic monolithic arches initially subjected to self-weight only and subsequently to equivalent lateral inertial loading. Given that the seismic hazard on the Moon or Mars can be a challenge for structures [31,34,24] and that self-weight is reduced due to the reduced gravitational acceleration (although the inertia of the structure remains the same), the structural response will change accordingly as highlighted in Kalapodis et al. [25,26]. Hence, the paper proceeds with the

limit-state analysis of both circular and parabolic monolithic arches in low-gravity conditions, by assuming lower gravitational accelerations, $ag = \{0.17; 0.38\}g$ corresponding to the lunar and martian gravitational fields respectively. Finally, it concludes with a case study regarding the minimum thickness of a monolithic semicircular and parabolic arch on the lunar surface. It is out of the scope of this paper to assess the effect of shear forces on the minimum thickness of the arches in reference.

2. Background of the problem

Engineers and researchers in the past have investigated the static behaviour of masonry arches but mostly focussing on semicircular arches ([30,22,27,3,41,45,16], amongst others). However, there were researchers that progressed with the investigation of other geometries of arches such as parabolic [41,39], elliptical [1], pointed/gothic [32,42,39] and catenary arches [42,33]. Most of the studies concerned the static behaviour and stability of those arches through determining their corresponding upper and lower bound thrust lines. More specifically, Sacco [41] reviewed the thrust line equation for semicircular and parabolic arches when they were subjected to uniform and non-uniform vertical loading through a nonlinear constrained minimisation algorithm. His results focussed on the generation of different maximum and minimum thrust lines for both types of arches (amongst others) and, although he presented the catenary as an admissible thrust line for vertical loading, he arrived at the thrust line corresponding to a four-hinge mechanism for non-uniform vertical loading. Block [7] highlighted that there are infinite equilibrium states in an arch; however, the maximum and minimum thrust lines denote the upper and lower bounds for all the associated admissible thrust lines of any arch. More specifically, they denote the thrust lines that correspond to the maximum and minimum thrust transferred to the abutments (horizontal component of the reaction force) and are associated with a statically determinate (three-hinge) arch as shown in Fig. 2. Ricci et al. [39] proceeded with a thorough analytical calculation of the thrust line of a semicircular arch subjected to both vertical and inertial loading and the numerical estimation, through Point Collocation Method [21] and constrained optimisation, of the upper and lower limits of semicircular, parabolic and pointed (statically determinate) arches.

The next step is the estimation of their minimum thickness given a specific loading through limit-state analysis. Makris and Alexakis [27] confirmed Milankowitch’s [30] results about the dimensionless minimum thickness of semicircular arches which is $t/R = 0.1075$ (t : thickness, R : radius) using radial ruptures and $t/R = 0.1095$ using vertical ruptures when subjected to self-weight. This was achieved by the calculation of the limit thrust line that corresponds to a five-hinge mechanism (a four-hinge mechanism would not be possible due to symmetry) as shown in Fig. 3a. Subsequently, Alexakis and Makris [3] determined the minimum thickness of circular arches with different embrace angles subjected to both self-weight and inertial loading. Interestingly, this was found through a variational formulation and the application of the principal of potential energy which enabled the estimation of the minimum horizontal acceleration levels that convert the arch into a four-hinge mechanism as shown in Fig. 3b. Furthermore,

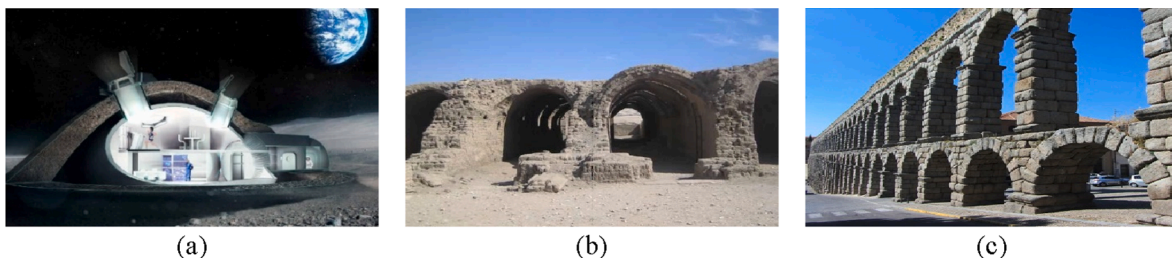


Fig. 1. (a) Section of a lunar module with a regolith arch shield from De Kestelier et al. [12]; (b) Ramesseum adobe vaults from AVN (2015); (c) Ancient Roman masonry aqueduct in Segovia from Rodrigues [40].

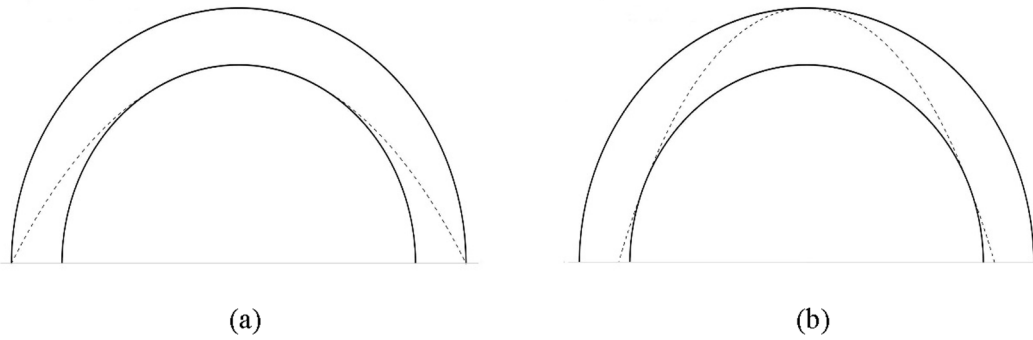


Fig. 2. Semicircular arch with its (a) maximum and (b) minimum thrust lines that correspond to a statically determinate structure under its' self-weight.

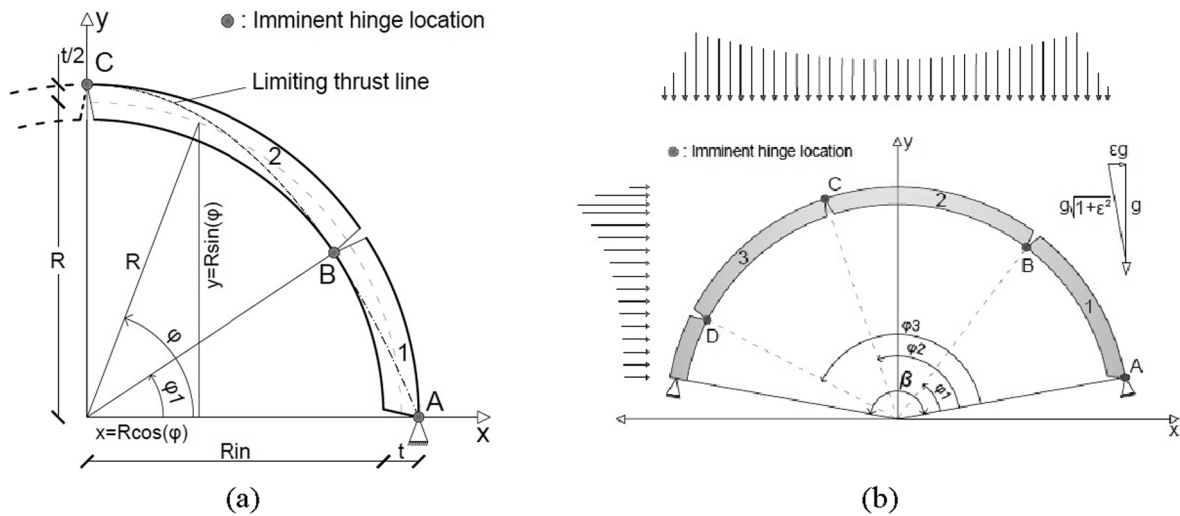


Fig. 3. (a) Right part of the five-hinge symmetrical mechanism for semicircular arches when subjected to their self-weight; (b) asymmetric four-hinge mechanism for circular arches with embrace angle β when subjected to both self-weight and inertial loading.

another important contribution was made by Nikolić [32] who managed to estimate the minimum thickness of pointed/gothic arches under self-weight just before turning into a five-hinge mechanism, using the thrust-line method.

After Hooke [20], the catenary shape symbolised the perfect arch shape as it represented the optimal thrust line. Gregory [19] proposed also the catenary shape as the thrust line that needs to fit within the intrados and extrados of any arch in order to stand. Nikolić [33] presented his work on the analytical expression of the thrust line of a catenary arch while he provided important insights into the equilibrium analysis of catenary arches with finite thickness subjected to their self-weight. In his thorough work, he highlighted the deviation of the resulting thrust line from the catenary centreline, however, he admits that there is no minimum thickness for a catenary arch under self-weight. When the thickness tends to zero (one-dimensional arch), the thrust line tends to follow a catenary shape and therefore will always be within the arch's geometry (intrados and extrados) – a very significant result, opposed to the other types of arches. Hence Nikolić [33] confirmed the idea of Hooke [20] and Gregory [19] that the catenary arches could potentially be the optimal arches under self-weight.

Subsequently, the scope of this paper is to implement limit-state analysis to parabolic arches, since they resemble to and are more common than catenary arches, for both self-weight and inertial loads. The investigation will be extended to low-gravity conditions as there is a need to provide useful insights and solid information about the stability and resilience of “extraterrestrial” arches acting as shielding structures for valuable assets on the Moon and Mars [44,24]. These regolith-based arches are assumed to work as monoliths independent of the

construction method (additive manufacturing, interlocking bricks, etc) at this stage. Therefore, limit-state analysis is an appropriate method since the new material will most probably be brittle, with adequate compressive strength but low tensile strength as mentioned above [9,18]. Additionally, no shear failure of the material is considered (including sliding at the base) and therefore only formation of radial hinges is allowed to take place anywhere along the arch. The effect of stereotomy is out of the scope of this paper, although it is an important factor affecting the minimum thickness required for the protection from extreme radiation.

The inspiration behind this section lies in Fig. 4. This figure shows roughly the same thrust line (black dashed line) which is expressed with a catenary shape (that bears great resemblance to the real thrust lines, even though it is not an admissible one) marginally fitted within both a semicircular and a parabolic (grey-scaled lines) arch under self-weight only. Evidently, there are two main qualitative conclusions that can be drawn from Fig. 4: (a) the five-hinge mechanism of the parabolic arch is exactly opposite than that of the semicircular and (b) the parabolic arch is much thinner compared to the semicircular. This latter point was an anticipated result following Nikolić's [33] insightful conclusions, since the parabolic resembles the catenary arch [17]. Hence, the structure in reference is a parabolic arch with $c = 1/2$ (as shown in Fig. 5a). This aspect ratio is particularly of interest, since it is directly comparable to semicircular arches.

Section 2.1 presents the analytical formulation of the symmetric five-hinge mechanism due to self-weight for the parabolic arch as shown in Fig. 5a. Due to the lack of pertinent literature, the results were validated using an independent numerical method developed by the authors in

2.1.2. Weight of an arbitrary segment of the parabolic arch

The next step is to consider a parabolic arch (r, t, β) with mid-thickness radius r , thickness t and embrace angle β . There are three different approaches for describing the geometry of a parabolic arch; however, this is not the case for elliptical and circular arches as they conclude to the same arch geometry. According to the first approach, each point of the intrados/extrados of the arch maintains a constant distance $t/2$, perpendicular to the centreline. The second approach (which is adopted in this work) considers the intrados/extrados lines to be radially proportional to the centreline (see Eqs. (A1), (A2) in the Appendix A) and therefore retains a constant t/r for all the range of φ_i angles. Finally, based on the third approach, each point of the extrados/intrados is at a constant radial distance $t/2$ from the centreline (not constant t/r for all the range of φ_i angles). As a result, for the first and third case, the intrados/extrados are not described by a purely parabolic shape. The three aforementioned approaches are depicted in Fig. 6.

This study adopts the second definition as described above where the parabolic arch keeps a constant t/r along its arc.

2.1.3. Moment equilibrium at the onset of the five-hinge mechanism

It has been shown graphically that a parabolic arch subjected to only self-weight, develops an opposite five-hinge mechanism to the corresponding semicircular arch as depicted in Fig. 4. More specifically, it is evident that the imminent hinges (at a state of equilibrium) of the collapse mechanism of the parabolic arch will appear at the intrados, where they would appear at the extrados for a semicircular arch and vice versa (Figs. 3a and 5a). This result follows Coulomb's [10] observation that the hinging mechanism depends on the upper and lower limits of the thrust force exerted at the crown. The symmetric right part of the collapse mechanism is depicted in Fig. 7a.

Furthermore, there is a need to define the gravitational multiplier, $\alpha = g'/g$, as the ratio of the gravitational acceleration on other planetary surfaces, g' , over the reference gravitational acceleration on Earth, $g = 9.81 \text{ m/s}^2$, in order to account for the different gravitational environments. Additionally, the factor, $L = m_{total}/m_{inertial}$, is defined as the ratio between the total mass of the structure and the additional infill, $m_{total} =$

$m_{structure} + m_{infill}$, over the mass that accounts for the inertial loading, $m_{inertial}$, which is part of m_{total} . This ratio seems to play a key role in the response of the arch. However, for terrestrial applications ($\alpha = 1$) the total mass, $m_{total} = m_{structure} = m_{inertial}$, is structural (no extra infill) and therefore it contributes fully to the inertial loads, $L = 1$.

By applying a moment equilibrium on the half-arch about the point A, the minimum horizontal thrust at the intrados of the crown, T , is determined. In order to take low gravity (α) and additional vertical (shielding) loading (L) factors into consideration, the weight of the segment (1-2) is taken equal to αLW_{12} . The equation of moment equilibrium is presented below as,

$$\begin{aligned} \text{Segment(1-2)} : T \left(\left\{ R - \frac{t}{2} \right\} - \sin(\beta_0) \left\{ r_0 - \frac{t}{2} \right\} \right) \\ - \alpha LW_{12} \left(\cos(\beta_0) \left\{ r_0 - \frac{t}{2} \right\} - x_{c12} \right) \\ = 0 \\ \Rightarrow T = \frac{\alpha LW_{12} \left(\cos(\beta_0) \left\{ r_0 - \frac{t}{2} \right\} - x_{c12} \right)}{\left\{ R - \frac{t}{2} \right\} - \sin(\beta_0) \left\{ r_0 - \frac{t}{2} \right\}}, \beta_0 \neq \frac{\pi}{2} \end{aligned} \quad (6)$$

where W_{12} (weight of half the arch) and x_{c12} (abscissa of the center of gravity of the half arch) are evaluated by the Eq. (A5) and Eq. (A6a) (of the Appendix A) respectively, with the assumption of $\varphi_i = \beta_0$ and $\varphi_{i+1} = \frac{\pi}{2}$. Furthermore, r_0 (radius at an angle β_0) is evaluated by the Eq. (5) for $\varphi_i = \beta_0$.

When assuming a radial rupture as shown in Fig. 7a, moment equilibrium of the upper portion (segment 2) of the arch about hinge B yields:

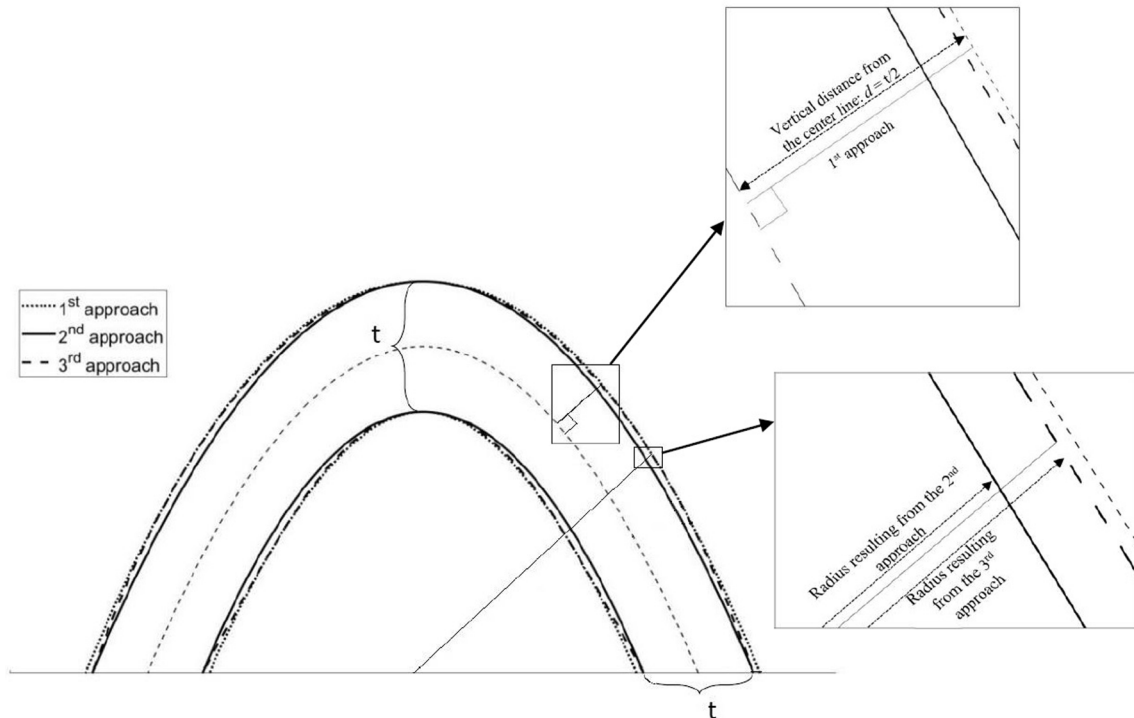


Fig. 6. Three different definitions for the description of a parabolic arch.

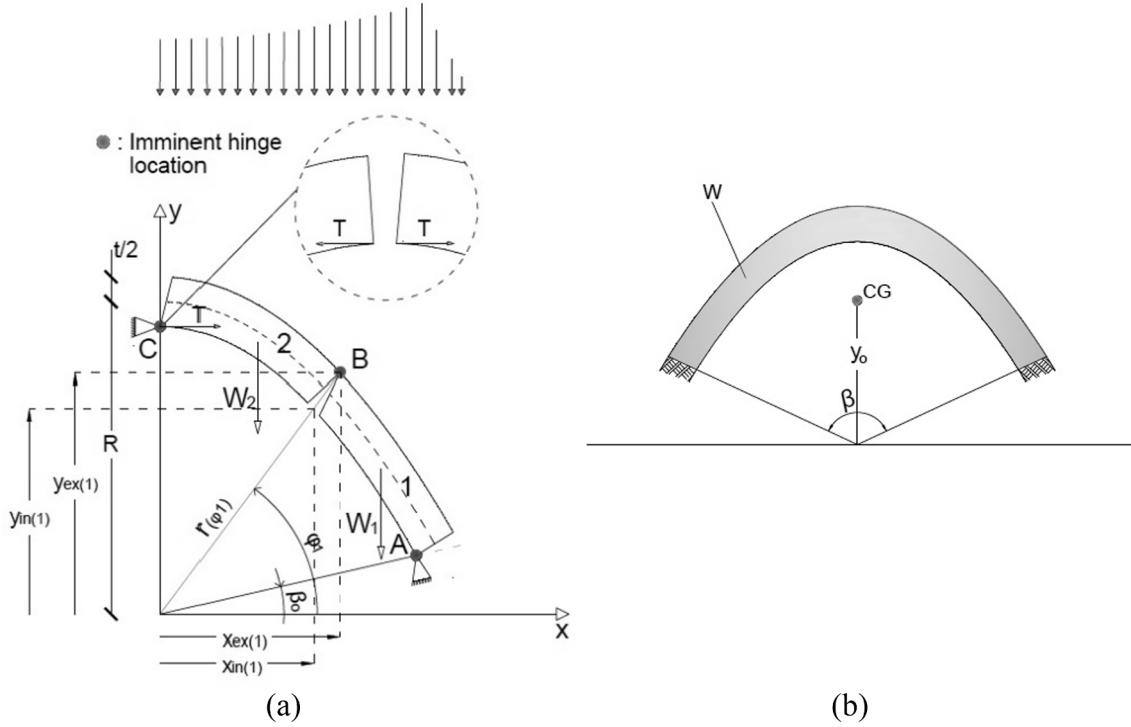


Fig. 7. (a) System of reference of the right symmetric part of the collapse mechanism of a parabolic arch subjected only to its self-weight and (b) ordinate of the centre of gravity of a parabolic arch with the consideration of an embrace angle β .

$$\begin{aligned}
 \text{Segment(2)} : & -\alpha L W_2 \left(\cos(\varphi_1) \left\{ r_{(\varphi_1)} + \frac{t}{2} \right\} - x_{c2} \right) + T \left(\sin(\varphi_2) \left\{ r_{(\varphi_2)} - \frac{t}{2} \right\} \right. \\
 & \left. - \sin(\varphi_1) \left\{ r_{(\varphi_1)} + \frac{t}{2} \right\} \right) \\
 = 0 \Rightarrow & -\alpha L W_2 \left(\cos(\varphi_1) \left\{ r_{(\varphi_1)} + \frac{t}{2} \right\} - x_{c2} \right) \\
 & + \frac{\alpha L W_{12} \left(\cos(\beta_0) \left\{ r_0 - \frac{t}{2} \right\} - x_{c12} \right)}{\left\{ R - \frac{t}{2} \right\} - \sin(\beta_0) \left\{ r_0 - \frac{t}{2} \right\}} \left(\left\{ R - \frac{t}{2} \right\} - \sin(\varphi_1) \left\{ r_{(\varphi_1)} \right. \right. \\
 & \left. \left. + \frac{t}{2} \right\} \right)
 \end{aligned} \tag{7}$$

where W_2 (weight of segment 2) and x_{c2} (abscissa of the center of gravity of the segment 2) are evaluated by the Eq. (A5) and Eq. (A6a) (of the Appendix A) respectively, with the assumption of $\varphi_i = \varphi_1$ and $\varphi_{i+1} = \frac{\pi}{2}$. Furthermore, $r_{(\varphi_1)}$ (radius at an angle φ_1) is evaluated by Eq. (5) for $\varphi_i = \varphi_1$.

By solving Eq. (7) with respect to t , a transcendental equation which relates the unknown rupture angle φ_1 with the unknown minimum thickness t is found. The general form of this equation is given below:

$$t = f(\varphi_1) \tag{8}$$

Adopting as a reference level the horizontal axis $x(y = 0)$, the potential energy of the parabolic arch with an embrace angle β (Fig. 7b) will be,

$$V = W_{arch} \cdot y_0 \tag{9}$$

where W_{arch} (weight of the parabolic arch) and y_0 (ordinate of the center of gravity of the parabolic arch) are evaluated by Eq. (A5) and Eq. (A6b) (of the Appendix A) respectively, with the assumption of $\varphi_i = \beta_0$ and $\varphi_{i+1} = \pi - \beta_0$. By substituting Eq. (8) in Eq. (9), we have

$$V(\varphi_1) = W_{arch} \cdot y_0 \tag{10}$$

According to the principle of stationary potential energy, the

geometrically admissible hinge mechanism shown in Fig. 5a is in an equilibrium state if and only if the total potential energy is stationary, i. e.,

$$\delta V(\varphi_1) = 0 \Rightarrow \frac{dV(\varphi_1)}{d\varphi_1} \delta\varphi_1 = 0 \Rightarrow \frac{dV(\varphi_1)}{d\varphi_1} = 0 \tag{11}$$

The solution of the system of Eqs. (8) and (11) yields the unknown location of the rupture angle φ_1 and the minimum width t of a parabolic arch with an embrace angle β .

2.2. Numerical methodology

An independent numerical method was developed to compute the corresponding limit thrust lines of different arches under different loading scenarios only in order to validate the analytical expressions presented above and to assist with the visualisation of the different failure mechanisms. To this end, an estimate of a monolithic arch's thrust line can be obtained through finding the thrust line of a highly discretised voussoir arch. Makris and Alexakis [27] defined the thrust line as the geometrical locus of the application points of the resultant thrust-force that develops at any joints of the arch. Representing the geometry with discrete segments will enforce that these application points lie on adjacent edges between voussoirs. For direct comparison with and validation of the variational method's results, radial cuts have been considered in this section.

To obtain physically admissible thrust lines the assumed set of thrust forces must result in the thrust line remaining within the intrados and extrados of the arch throughout its length. A numerical approach to finding the correct set of resultant thrust forces corresponding to an arch's limit thrust line has been developed following the graphic statics approach employed by Block et al [7], Michiels et al. [28], Michiels and Adriaenssens [29], among others. The method constructs a force polygon from which a set of resultant thrust forces that satisfy horizontal and vertical equilibrium can be automatically obtained. A force polygon comprises of two components, the load line and the pole as shown in Fig. 8b. The load line represents the magnitude and direction of resultant

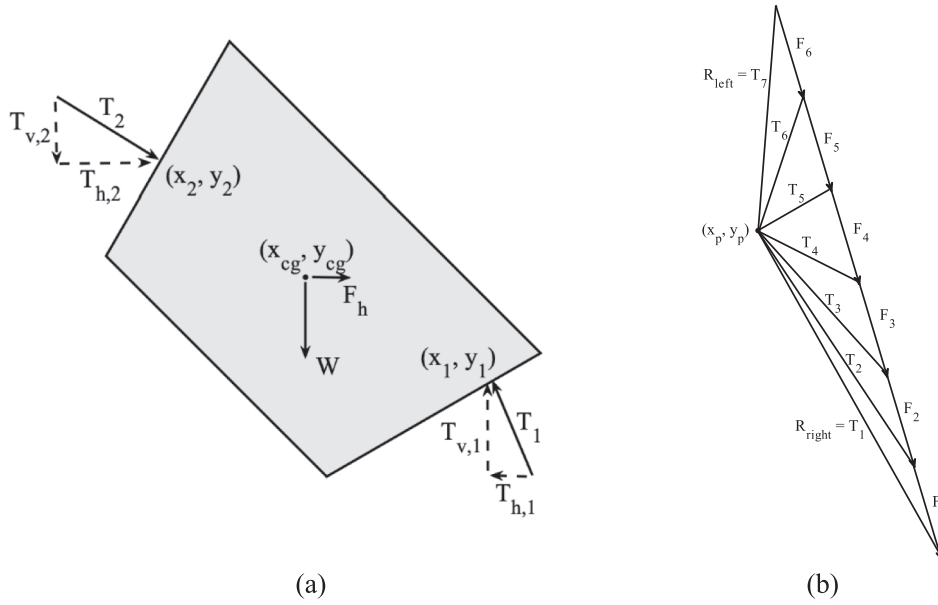


Fig. 8. (a) Static equilibrium of a single voussoir and (b) An example of a force polygon used to determine resultant thrust forces for an arch discretised into six voussoirs.

forces acting at the centroid of each voussoir. The lines that connect the pole to the vertices of the load line will then define the magnitude and direction of the resultant thrust forces. The first and last of these lines will represent the reaction forces at the left and right hand supports, hence by estimating these forces a force polygon can be constructed. In this case, an initial estimate of the reaction forces is calculated using a virtual work method, by assuming a uniform flexural rigidity and that internal deformations are dominated by bending. By setting the pole of the force polygon at (0,0) in force space, the estimated reactions can then be used to trace the load line.

Once the initial force polygon has been obtained, the resultant thrust forces can be inferred from it and an initial estimate of the thrust line can be obtained by assuming a starting position (right hand side). The estimate of the reactions is taken at the centre of the supports by assuming a flexural arch, with uniform flexural rigidity. As in reality the arch is closer to rigid, the initial estimate of the reaction forces is unlikely to yield an admissible thrust line. Thus, initially, the vertical position of the force polygon pole is adjusted such that the end point (left hand side) of the thrust line lands in the desired position. The horizontal thrust of the system is sought such by adjusting the horizontal position of the pole in order to ‘flatten out’ the thrust line until an admissible line is found. An outline of the algorithm employed to compute the limit thrust line is given in Fig. 9.

2.3. Results

Fig. 10 presents a comparison between the limit thrust lines for semicircular and parabolic arches with embrace angle $\beta = 180^\circ$ under their self-weight. As anticipated, it is observed that the collapse mechanisms are exactly opposite; in the case of the semi-circular arch, the thrust line starts at the extrados at the base, it touches the intrados at 35.52° and then the extrados at the crown, while for the parabolic arches the limit thrust line starts at the intrados, at the base, then touches the extrados at 43.81° and the intrados at the crown. The fact that the rupture angles of the parabolic arch are “higher” (longer legs) compared to the semicircular arch further highlights the pattern of the opposite mechanisms. A very important result is that the minimum thickness of parabolic arches is $t/R = 0.0239$, while the corresponding minimum thickness for semicircular arches is $t/R = 0.1075$. This is another significant difference showcasing quantitatively the “geometrical

favouritism” towards structures that resemble the catenary [33], as shown qualitatively in Fig. 4. The numbering adopted for the rupture angles is different between the circular and parabolic arches to facilitate comparison; this will become evident in the next section when accounting for inertial loading.

Fig. 11a compares the minimum dimensionless thickness of circular to parabolic arches for different embrace angles, β . Evidently, the parabolic arches (with $c = 1/2$), always require thinner geometries to support their self-weight than their circular counterparts, regardless of β . Furthermore, the difference between the $\min(t/R)$ of a circular and parabolic arch decreases for smaller values of β (Fig. 11a). It is important to note here that for constant (locked) c , when the embrace angle decreases, it results in an arch with smaller arc. Following this observation and Fig. 11b it can be deduced that as the embrace angle decreases (smaller arcs) the whole collapse mechanism is “lifted up” resulting in thinner geometries.

3. Identification of the four-hinge mechanism for parabolic arches subjected to inertial loading

When an arch is subjected to a horizontal acceleration, it exhibits a four-hinge asymmetric mechanism as highlighted by Alexakis and Makris [3] amongst others. Fig. 12 presents a comparison between the two different limit thrust lines for semicircular and parabolic arches under their self-weight and a horizontal acceleration of 0.05 g (from left to right) revealing the different developed mechanisms. As in the case of the five-hinge mechanism of the previous section, it is evident that the mechanisms are exactly opposite. More specifically, for the semi-circular arch, the limit thrust line starts at the extrados at the right abutment (for left to right acceleration), then touches the intrados at $\varphi_1^C = 37.18^\circ$, the extrados at $\varphi_2^C = 92.86^\circ$, and finally the intrados at $\varphi_3^C = 148.54^\circ$. However, for parabolic arches the limit thrust line starts at the intrados of the left abutment (for left to right acceleration), then touches the extrados at $\varphi_1^P = 180^\circ - 46.69^\circ$, the intrados at $\varphi_2^P = 180^\circ - 94.08^\circ$, and finally the extrados at $\varphi_3^P = 180^\circ - 160.32^\circ$, as shown in Fig. 10b. To facilitate comparisons between the different failure mechanisms of the two types of arches studied in this paper, the following assumptions regarding the rupture angles have been made. In the case of circular geometry, $\varphi_1 = \varphi_1^C$, $\varphi_2 = \varphi_2^C$ and $\varphi_3 = \varphi_3^C$; for the parabolic geometry, $\varphi_1 = \pi - \varphi_1^P$, $\varphi_2 = \pi - \varphi_2^P$ and $\varphi_3 = \pi - \varphi_3^P$.

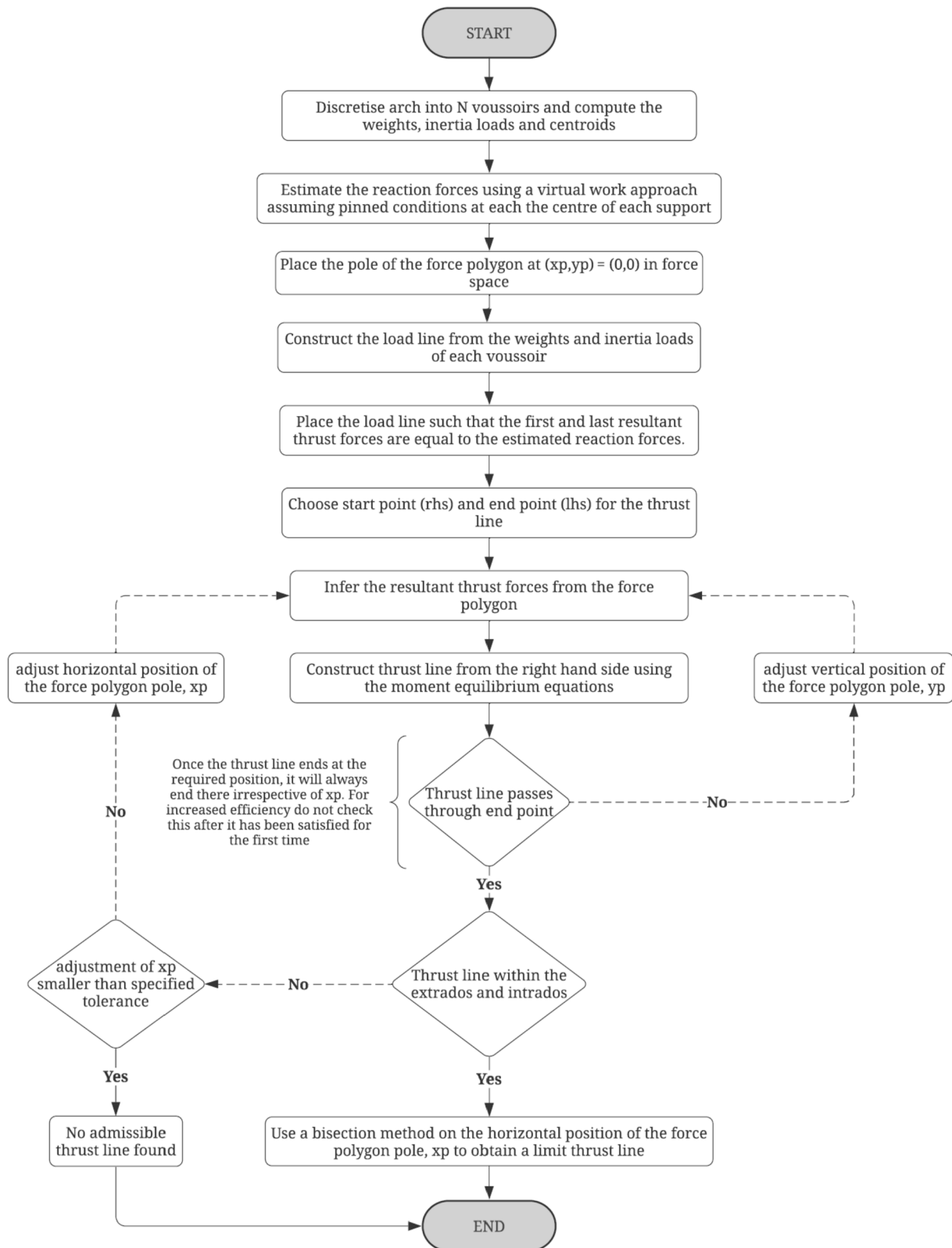


Fig. 9. Overview of limit thrust line algorithm.

Fig. 13 compares the two asymmetric collapse mechanisms for a circular (Fig. 13a) and a parabolic arch (Fig. 13b) and show explicitly the convention of numbering the rupture angles. Fig. 13b also reveals the moment equilibrium at the onset of the four-hinge mechanism of the parabolic arch.

3.1. Moment equilibrium at the onset of the four-hinge mechanism

Once the equations of the centres of gravity for the four segments that correspond to the five-hinge mechanism have been evaluated, a moment equilibrium of segment 2 about point B is applied (as shown in

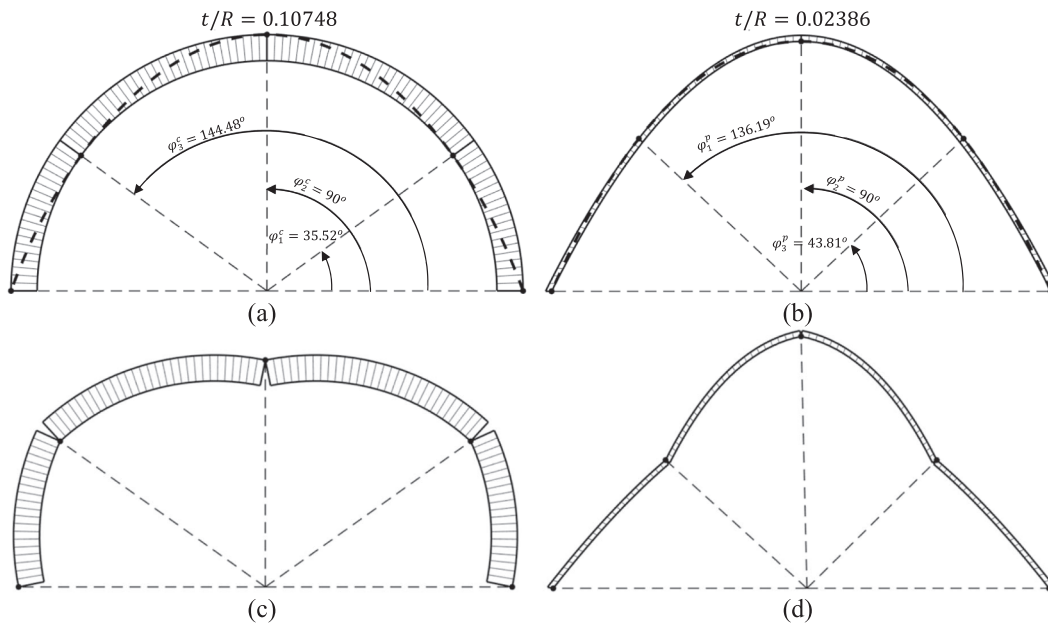


Fig. 10. Limit thrust line for (a) semicircular and (b) parabolic arches; symmetric five-hinge mechanism of (c) semicircular and (d) parabolic arches when subjected to their self-weight.

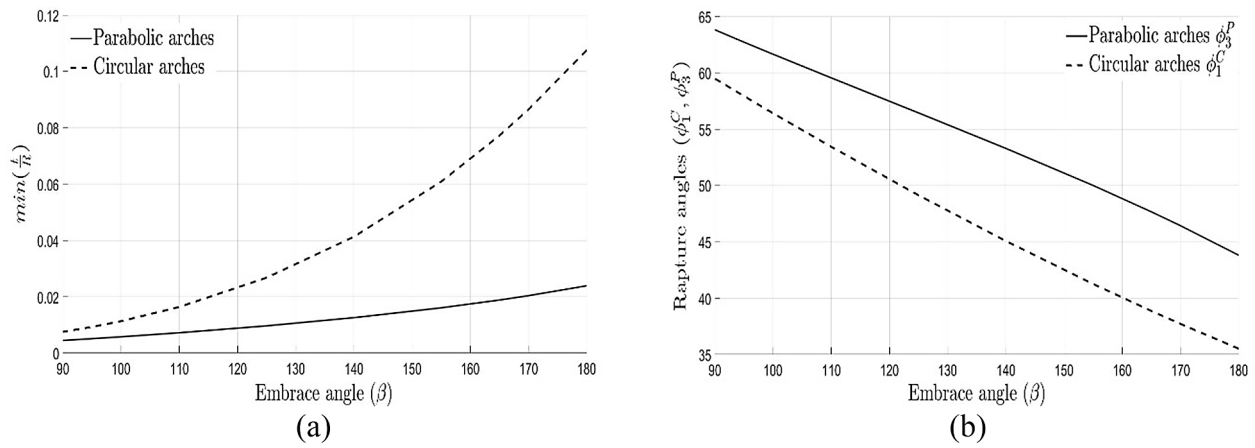


Fig. 11. (a) Minimum t/R and (b) intermediate rupture angle (ϕ_1^c for circular, ϕ_3^p for parabolic) versus various embrace angles (β) for circular (solid line) and parabolic arches (dashed line) subjected only to their self-weight.

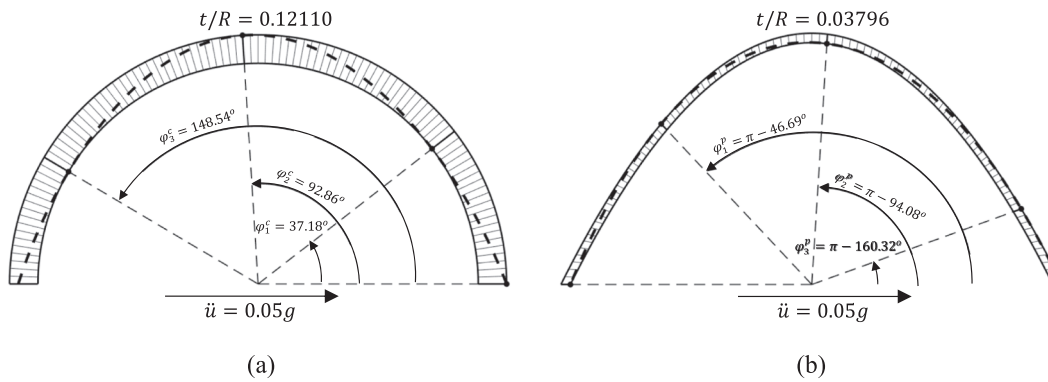


Fig. 12. Limit thrust lines of a (a) semi-circular and (b) parabolic arch subjected to their self-weight combined with an inertial lateral load of 0.05 g, posed from left to right.

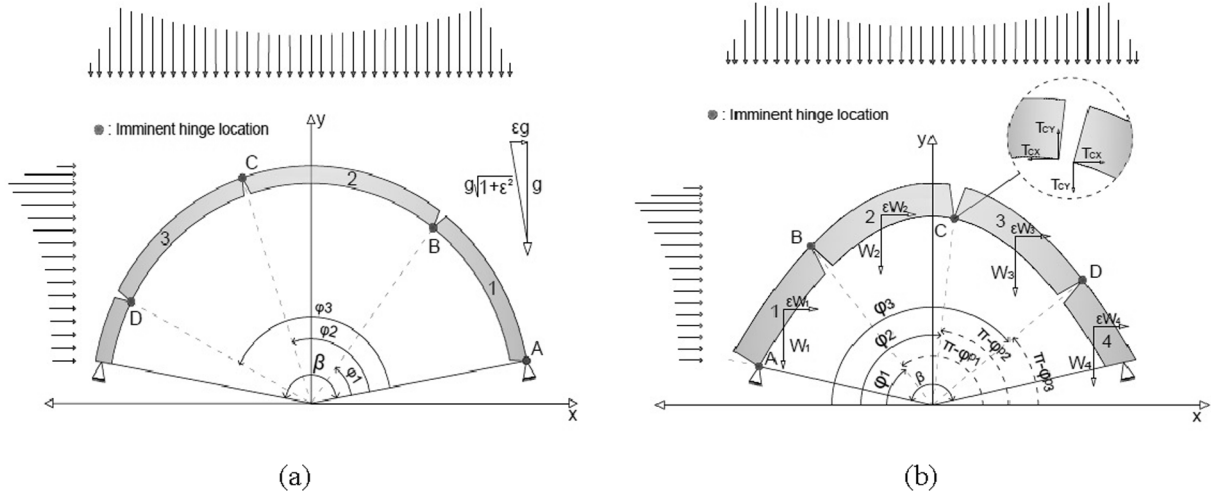


Fig. 13. Four-hinge collapse mechanisms for (a) a circular and (b) a parabolic arch subjected to self-weight and inertial loading. Notice the difference in the convention of numbering the rupture angles.

Fig. 13b). In order to consider low gravity (α) and the extra additional loading (L), all the weights of the segments are multiplied by αL .

$$\begin{aligned} \text{Segment(2)} : & -\varepsilon W_2 \left(y_{c2} - \sin(\varphi_1) \left\{ r_1 + \frac{t}{2} \right\} \right) - \alpha L W_2 \left(\cos(\varphi_1) \left\{ r_1 + \frac{t}{2} \right\} \right. \\ & \left. - x_{c2} \right) + T_{cx} \left(\sin(\varphi_2) \left\{ r_2 - \frac{t}{2} \right\} - \sin(\varphi_1) \left\{ r_1 + \frac{t}{2} \right\} \right) \\ & + T_{cy} \left(\cos(\varphi_1) \left\{ r_1 + \frac{t}{2} \right\} - \cos(\varphi_2) \left\{ r_2 - \frac{t}{2} \right\} \right) \\ & = 0 \end{aligned} \quad (12)$$

Similarly, moment equilibrium of segment 3 about point D is applied:

$$\begin{aligned} \text{Segment(3)} : & -\varepsilon W_3 \left(y_{c3} - \sin(\varphi_3) \left\{ r_3 + \frac{t}{2} \right\} \right) + \alpha L W_3 \left(x_{c3} \right. \\ & \left. - \cos(\varphi_3) \left\{ r_3 + \frac{t}{2} \right\} \right) - T_{cx} \left(\sin(\varphi_2) \left\{ r_2 - \frac{t}{2} \right\} \right) \\ & - \sin(\varphi_3) \left\{ r_3 + \frac{t}{2} \right\} + T_{cy} \left(\cos(\varphi_2) \left\{ r_2 - \frac{t}{2} \right\} \right) \\ & - \cos(\varphi_3) \left\{ r_3 + \frac{t}{2} \right\} \\ & = 0 \end{aligned} \quad (13)$$

where ε is the horizontal acceleration coefficient, L is the weight multiplier and α the gravitation multiplier. Their value is $\alpha = L = 1$ in this section, however, those parameters will be further discussed in the next section.

By solving Eqs. (12) and (13), the moment equilibrium of Segment 1–2 about the point A can be expressed in terms of T_{cx} , and T_{cy} :

$$\begin{aligned} \text{Segment(1-2)} : & T_{cx} \left(\sin(\varphi_2) \left\{ r_2 - \frac{t}{2} \right\} - \sin(\beta_0) \left\{ r_0 - \frac{t}{2} \right\} \right) \\ & + T_{cy} \left(\cos(\beta_0) \left\{ r_0 - \frac{t}{2} \right\} - \cos(\varphi_2) \left\{ r_2 - \frac{t}{2} \right\} \right) \\ & - \varepsilon W_{12} \left(y_{c12} - \sin(\beta_0) \left\{ r_0 - \frac{t}{2} \right\} \right) \\ & - \alpha L W_{12} \left(\cos(\beta_0) \left\{ r_0 - \frac{t}{2} \right\} - x_{c12} \right) \\ & = 0 \end{aligned} \quad (14)$$

Eq. (14) can be re-solved for ε :

$$\varepsilon = f(\varphi_1, \varphi_2, \varphi_3, t) \quad (15)$$

To calculate the rupture angles, $\varphi_1, \varphi_2, \varphi_3$ that correspond to minimum t/R for a given horizontal acceleration level, ε , the principle of potential energy is employed [3]. This constitutes an alternative way that deviates from the need to calculate analytically the limit thrust line

which can become very complex—especially for geometries with varying curvature such as the parabolic arches [39].

As abovementioned, the entire energy of the system is expressed as the work of all forces acting on the structure with reference $y = 0$. The loading on a parabolic arch subjected to a horizontal acceleration, εg , is equivalent to the gravity loading on the same parabolic arch when it is rotated by an angle, $\omega = \tan^{-1} \varepsilon / \alpha$ from the vertical under a new gravitational field, $\hat{g} = g\sqrt{\alpha^2 + \varepsilon^2}$. Fig. 14 shows the new, tilted system where the resultant gravitational field is \hat{g} and the potential energy can be expressed as

$$\hat{V} = \hat{W} \cdot \hat{y} = \sqrt{\alpha^2 + \varepsilon^2} W \hat{y} \neq V \quad \text{or}$$

$$V(\varphi_1, \varphi_2, \varphi_3, \varepsilon) = \sqrt{1 + f(\varphi_1, \varphi_2, \varphi_3, t)^2} W \hat{y} \quad (16)$$

The principle of potential energy dictates that the four-hinge mechanism is a natural state (in equilibrium) among all geometrically admissible states of the system if, and only if, the variational work increment vanishes for arbitrary geometrically admissible variations. Therefore, the potential energy of the system needs to be stationary, $\delta V = 0$ [3].

The potential energy is stationary when:

$$\delta V = V(\varphi_i \pm \delta \varphi_i) - V(\varphi_i) = \frac{\partial V(\varphi_i, \varepsilon)}{\partial \varphi_i} \delta \varphi_i = 0 \Rightarrow \frac{\partial V(\varphi_i, \varepsilon)}{\partial \varphi_i} = 0$$

This yields the following set of equations:

$$\frac{\partial V(\varphi_1, \varphi_2, \varphi_3, \varepsilon)}{\partial \varphi_1} = 0 \quad (17a)$$

$$\frac{\partial V(\varphi_1, \varphi_2, \varphi_3, \varepsilon)}{\partial \varphi_2} = 0 \quad (17b)$$

$$\frac{\partial V(\varphi_1, \varphi_2, \varphi_3, \varepsilon)}{\partial \varphi_3} = 0 \quad (17c)$$

where by substituting Eq. (16) into Eq. 17a, b, c :

$$\begin{aligned} \frac{\partial V(\varphi_1, \varphi_2, \varphi_3, \varepsilon)}{\partial \varphi_i} &= \frac{\partial f(\varphi_1, \varphi_2, \varphi_3, t)}{\partial \varphi_i} W \hat{y} \frac{f(\varphi_1, \varphi_2, \varphi_3, t)}{\sqrt{1 + f(\varphi_1, \varphi_2, \varphi_3, t)^2}} = 0 \quad i \\ &\in [1, 2, 3] \end{aligned} \quad (18)$$

Given that the horizontal acceleration is not zero, $\varepsilon = f(\varphi_1, \varphi_2, \varphi_3, t) \neq 0$, and that \hat{y} is also nonzero, Eq (18) yields:

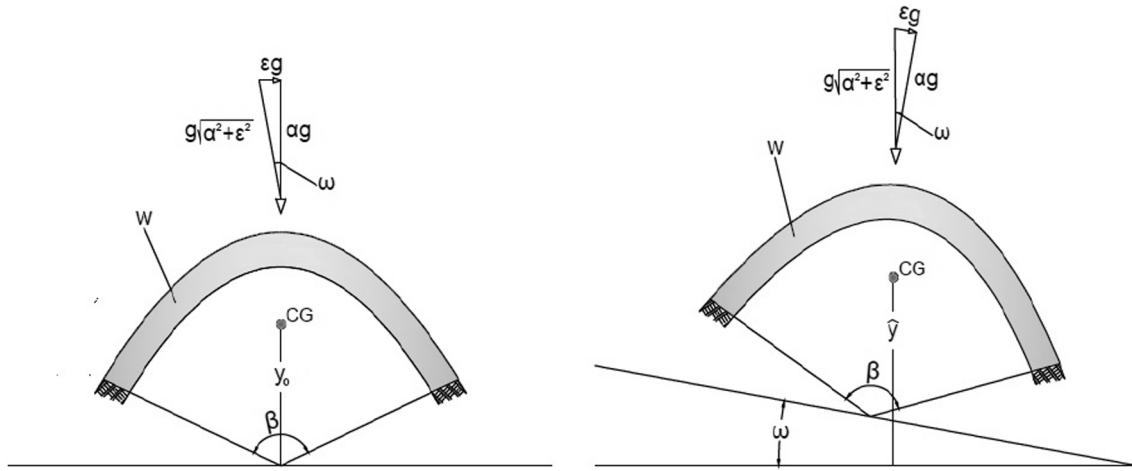


Fig. 14. Tilted system with a new resultant gravitational field equal to $\hat{g} = g\sqrt{\alpha^2 + \varepsilon^2}$.

$$\frac{\partial f(\varphi_1, \varphi_2, \varphi_3, t)}{\partial \varphi_i} = \frac{\partial \varepsilon}{\partial \varphi_i} = 0 \quad (19)$$

Eq (15) together with expression (19) for $i \in [1, 2, 3]$ offer a 4×4 equation system that can be solved in order to calculate the four unknowns $\varphi_1, \varphi_2, \varphi_3$ and t for a given acceleration level and embrace angle β . Fig. 15 shows the different limit thrust lines for semicircular and parabolic arches under their self-weight and horizontal accelerations, $\varepsilon g = \{0.1; 0.2; 0.4; 0.6\}g$ together with the corresponding rupture angles. For a horizontal force acting from left to right, the failure mechanism always starts from the intrados at the left abutment, φ_1 is located at the extrados, φ_2 at the intrados and φ_3 at the extrados.

Fig. 16 shows also a comparison between the analytical and numerical results regarding the minimum thickness of the parabolic arches under self-weight and different horizontal acceleration levels. It can be appreciated that the results are very close and provide an appropriate validation of the analytical calculations.

3.2. Minimum thickness and imminent hinge locations of circular and parabolic arches

The minimum thickness and the hinge locations of the parabolic and circular arches are presented in Fig. 17 and Fig. 18 respectively for terrestrial gravitational conditions ($\alpha = 1$) and with the consideration that all of the mass contributes to inertial forces ($L = 1$). As expected, Fig. 17 clearly depicts i) the need for thicker geometries as the lateral inertial load increases and ii) the need for thinner geometries as the embrace angle decreases as it corresponds to smaller arches, for both the circular and parabolic case. However, contrary to the self-weight consideration where the parabolic arches have been proved more optimal than the corresponding circular ones (as shown in Fig. 11a), Fig. 17 indicates that after a certain value of embrace angle (β) and lateral inertial load (εg), the circular arches tend to be more efficient. More specifically, for $\beta = \{125^\circ, 90^\circ\}$ the circular arches constitute a better choice for lateral loading higher than those corresponding to 0.225 g and 0.064 g, respectively. One reason behind this interesting observation is that as the embrace angle decreases, both types of arches have smaller arcs; however, the parabolic has a “steeper” top part compared to the circular arch that has a “flatter” top part in order to accommodate more efficiently the shape of the limit thrust line.

Fig. 18 plots the rupture angles’ locations against the levels of horizontal acceleration for parabolic and circular arches with embrace $\{\beta = 90^\circ, 125^\circ, 155^\circ \text{ and } 180^\circ\}$. It should be noted here that from Figs. 12 and 15, the four-hinge mechanism of the parabolic arch follows a “downstream”/clockwise pattern (from left intrados to right extrados), while in the case of the circular arches the mechanism follows an “upstream”/

counterclockwise pattern (from right extrados to left intrados) for a lateral load from left to right. As aforementioned, following the numbering convention of Fig. 11 and for comparison reasons the hinge locations for the circular will be shown as $\varphi_i = \varphi_i^C$ and for the parabolic $\varphi_i = 180 - \varphi_i^P$. When it comes to parabolic arches, φ_3 reaches the extrados at the base for substantially lower values of inertial loading compared to the circular arches. Furthermore, φ_2 does not change significantly, especially for the case of parabolic arches across the whole range of lateral loading. Interestingly, particularly for the case of parabolic arches, as the lateral loading increases, φ_1 and φ_2 increase up to a point (move clockwise) before they start decreasing again (move counterclockwise). On the other hand, φ_1 and φ_2 of the circular arches, are constantly increasing. Another observation is that as the embrace angle is decreasing, φ_1 is increasing and φ_3 is decreasing in order to fit within the new smaller arch.

4. Minimum thickness and hinge locations of parabolic and circular arches in low-gravity conditions

This section discusses the effects of low gravity in the stability of parabolic and circular arches. The effect of low gravity is considered through the gravitational multiplier, $\alpha = g'/g$, that takes the values of 0.38 and 0.17 which correspond to the martian and lunar gravitational fields, respectively. However, given the concept that these arches can be used as potential shielding structures from radiation and extreme temperature fluctuations, there might be the need to add loose regolith material at the top in order to reach a certain protective thickness equal to 250 cm [6].

$L = \frac{m_{total}}{m_{inertia}} = \frac{m_{structure} + m_{infill}}{m_{inertia}}$ in this case accounts for the additional mass of the loose regolith infill, $m_{infill} \neq 0$, and since not all of it contributes to inertial loading, $m_{inertia}$, L can take the values, $L = 1, 2, 3, 4$ ($L = 1$ denotes that all the mass contributes to inertia, $m_{total} = m_{inertia}$). More specifically, Fig. 19 shows a rough representation of the “compacted” loose regolith infill atop of a parabolic arch. Fig. 19(a) shows the infill following the structure when subjected to more frequent, low-impact ground motions (similarly to Serviceability Limit State, SLS). In this case, $L = 1$, as the infill contributes fully to the inertia of the total structure. On the other hand, Fig. 19(b) shows the infill that has yielded, and has partially collapsed, when the structure is subjected to more significant ground motions (similarly to the Ultimate Limit State, ULS). In this case, the infill contributes only partially to the inertia of the structure, as it is not monolithically attached to it and therefore $L > 1$. There are many reasons for this partial collapse such as the intensity of the ground motion, the geometry of the arch, how the loose material has been attached upon the arch, the interface conditions between the loose

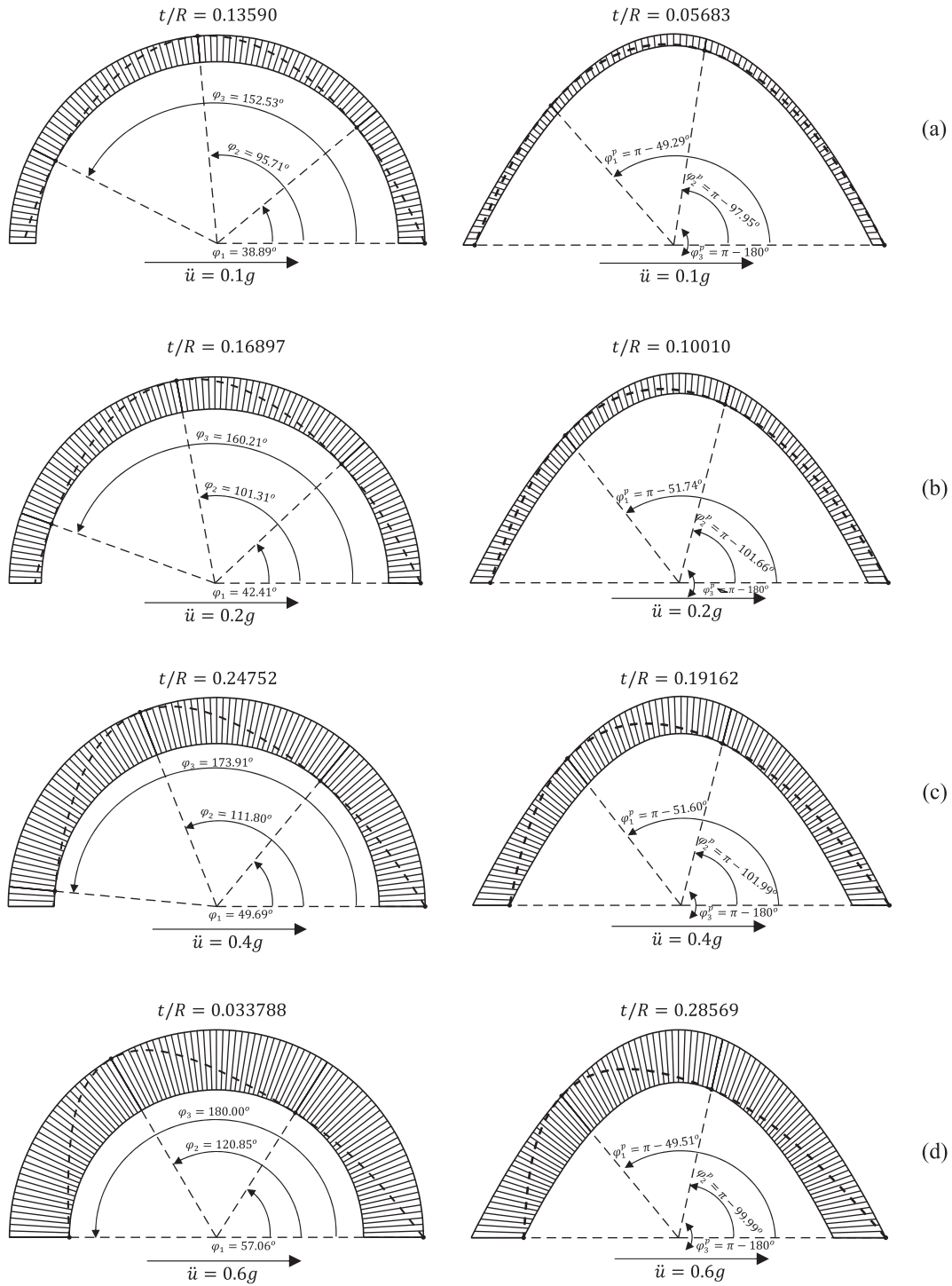


Fig. 15. Limit thrust lines for semicircular and parabolic arches under their self-weight and horizontal acceleration (from left to right) of (a) $\epsilon g = 0.1g$; (b) $\epsilon g = 0.2g$; (c) $\epsilon g = 0.4g$ and (d) $\epsilon g = 0.6g$.

and the structural material, the gravitational conditions, etc., and further investigation is needed when proceeding to the design of these arches.

Figs. 20 and 21 show the variation of the minimum thickness of circular and parabolic arches with embrace angles $\{\beta = 90^\circ, 125^\circ, 155^\circ \text{ and } 180^\circ\}$, when subjected to different levels of inertial loading in different gravitational fields, $\alpha = 1, 0.38, 0.17$, and different levels of L (i.e. $L = 1, 2, 3, 4$).

It is observed from these figures that the required minimum thickness increases with increasing lateral acceleration, however, it gets

further amplified as gravity decreases (lower α values). Moreover, the additional weight due to the protective shielding of an arch designed in low-gravity conditions (e.g. lunar surface) that does not contribute to inertial loading (L) will be beneficial in terms of structural material saving. As it was observed in the previous section, smaller embrace angles lead to thinner geometries. The same phenomenon takes place in low-gravity conditions. An indicative example to highlight the previous statement is that according to Fig. 20a, two circular arches with $L = 1$, constructed on the martian surface which have the same minimum thickness ($t/R = 0.2$) and different embrace angles ($\beta = 155^\circ, 125^\circ$) can

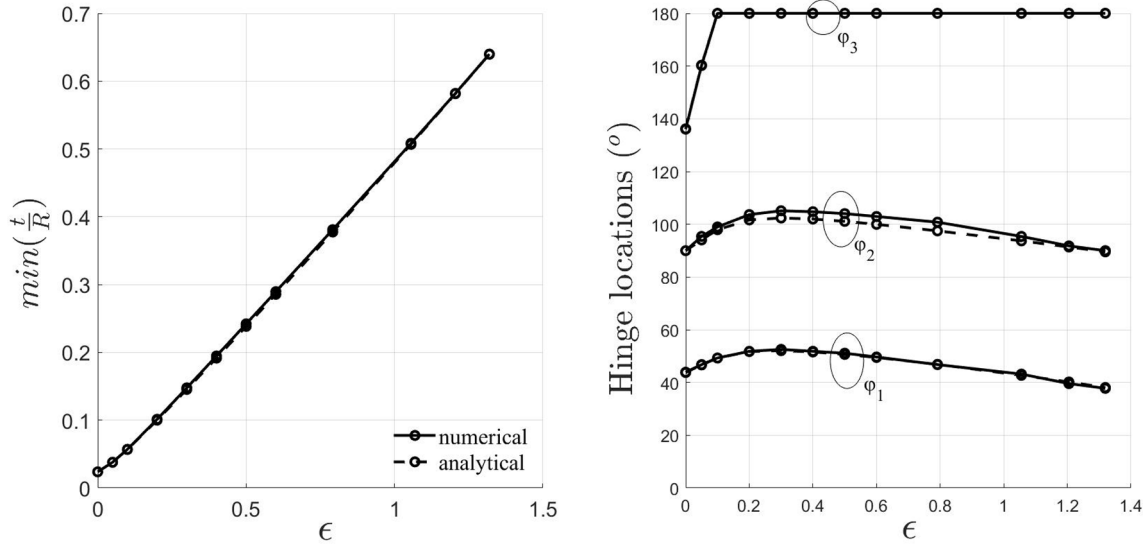


Fig. 16. Analytical versus numerical minimum thickness and hinge locations of parabolic arches when subjected to self-weight and horizontal acceleration.

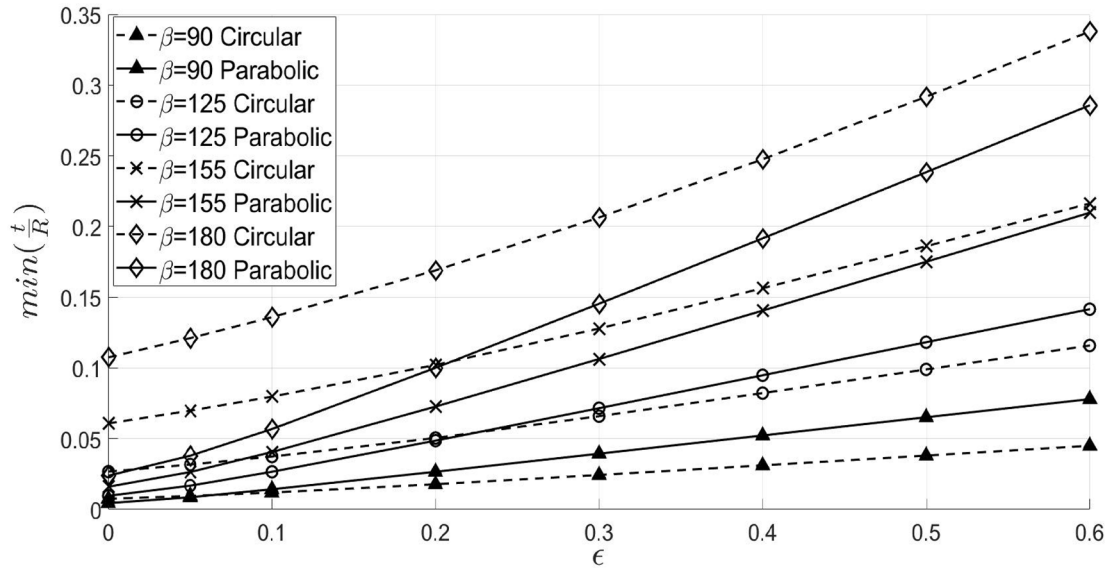


Fig. 17. Minimum t/R versus inertial acceleration for circular and parabolic arches with embrace angles $\{\beta = 90^\circ, 125^\circ, 155^\circ \text{ and } 180^\circ\}$.

sustain up to 0.2g and 0.42g respectively.

Fig. 22 shows the minimum thickness of parabolic and circular arches with different embrace angles varying with the different levels of horizontal acceleration considering low-gravity conditions and $L = 1$. It is evident that for an embrace angle $\beta = 180^\circ$, parabolic arches will always require less material than semicircular arches; however, this is not always the case for all embrace angles. For $\beta = 155^\circ$, after a certain level of horizontal acceleration the circular arch becomes more efficient. This effect is even more pronounced for arches with $\beta = 125^\circ, 90^\circ$ where the circular is almost universally more beneficial than the parabolic arch. Furthermore, it is important to observe how dominant is the effect of low gravity on the minimum required thickness for both types of arches –especially for $\beta = 180^\circ$. This is an anticipated conclusion as the stability of any arch depends heavily on gravity.

Interestingly, the phenomenon exhibits a self-similar behaviour presented via the master curves of the minimum t/R and rupture angles against the dimensionless horizontal acceleration, $\epsilon/\alpha L$ for both parabolic and circular arches in Figs. 23, 24. In particular, each pair of β and minimum t/R corresponds to a unique vector of $\{\epsilon/\alpha L, \varphi_1, \varphi_2, \varphi_3\}$.

According to Fig. 23, for high values of $\epsilon/\alpha L$ (which correspond to either substantial inertial loads or low-gravity conditions and more mass of the infill contributing to inertial loading) the parabolic arch can be always thinner than the circular arch for $\beta = 180^\circ$, however as the embrace angle reduces, there is a certain value of $\epsilon/\alpha L$ after which the circular arch becomes more efficient than the parabolic, following Fig. 22. These values of the dimensionless inertial loading with the associated values of the minimum required thickness against the different embrace angles are presented in Fig. 24. The areas where the parabolic or the circular arch is more efficient can be deduced explicitly from this figure. For $\beta = 180^\circ$, in all cases the parabolic arch is more beneficial. For arch geometries subjected to their self-weight only ($\frac{\epsilon}{\alpha L} = 0$) and for all the range of embrace angles β , the parabolic configuration is always more efficient, following Fig. 11a findings.

In the case of a lateral load, $\epsilon = 0.1$, on the lunar surface, $\alpha = 0.17$, with $L = 1$, the dimensionless inertial load will be $\frac{\epsilon}{\alpha L} = 0.59$. Thus, if an embrace angle of more than $\beta > 150^\circ$ is of interest, the parabolic geometry should be chosen, while if $\beta < 150^\circ$, the circular arch should be preferred. Furthermore, if the design thickness of the arch is pre-decided

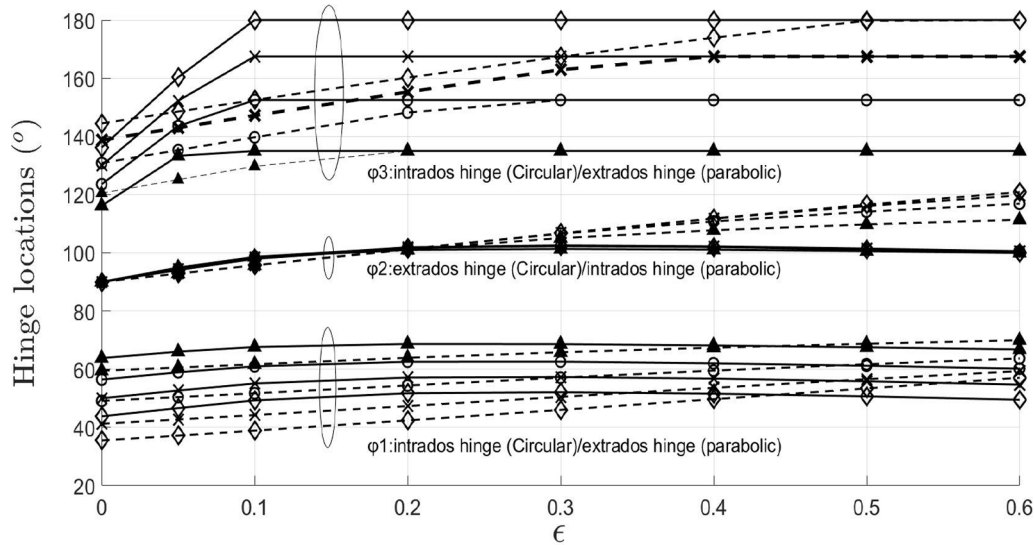


Fig. 18. Hinge locations versus inertial acceleration for circular and parabolic arches with embrace angles $\{\beta = 90^\circ, 125^\circ, 155^\circ \text{ and } 180^\circ\}$.

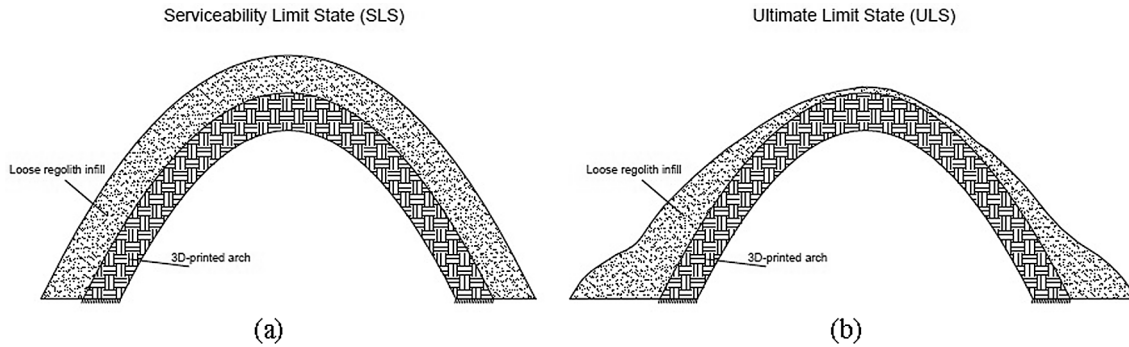


Fig. 19. Rough representations of a “compacted” loose regolith infill atop of a parabolic arch. (a) parabolic arch with a “loose” regolith infill during a frequent ground motion (SLS); (b) parabolic arch with asymmetrically yielded/collapsed “loose” regolith infill subjected to strong ground motion (ULS).

equal to be $\frac{t}{R} = 0.2$, for arches with an embrace angle $\beta > 150^\circ$ the parabolic geometries will sustain higher amount of dimensionless inertial loading $\frac{\epsilon}{\alpha L}$ than the corresponding circular ones. Evidently, Fig. 24 can be used for preliminary design decisions.

Fig. 25 illustrates the master curves for the rupture angles against the dimensionless inertial loading, $\frac{\epsilon}{\alpha L}$, for both parabolic and circular arches with embrace angles $\beta = 90^\circ, 125^\circ, 155^\circ \text{ and } 180^\circ$. The most significant similarity between the different types of arches is associated with the behaviour of the intermediate rupture angles, φ_1, φ_2 ; in both cases the hinges locations move more “upstream” (counterclockwise) against the load’s direction modifying the mechanism pattern in the same way following the findings of Fig. 15.

A summary of all the results is presented in Table A1, which is included as supplementary material in this paper. This table shows all the results produced by means of limit-state analysis for both circular and parabolic arch geometries. More specifically, Table A1 provides the minimum t/R and the corresponding rupture angles (that define the failure mechanism) for a plethora of combinations of (i) inertial acceleration amplitudes (ϵ), (ii) gravitational (α), (iii) self-weight multipliers (L) and (iv) embrace angles (β).

5. Case study

This last section presents a case study to illustrate the more practical aspects of the results obtained in the previous sections. The problem to be addressed herein is what would be the ideal arch (circular or

parabolic) that needs to cover a span of 30 m and a height of 15 m on the lunar surface ($\alpha = 0.17$). The selected arches would need to withstand a maximum (design) horizontal acceleration of 2 m/s^2 due to the imminent shallow moonquakes and meteoroid impacts, when the minimum required thickness of any lunar structure for shielding purposes is $t_{\text{radiation}} = 2.5 \text{ m}$ [6]. This level of acceleration can be expected after [34] that compare the magnitude-frequency relationships for shallow moonquakes and intraplate earthquakes in Central-Eastern US (CENA), showing that moonquakes with body-wave magnitude more than 5.5 had been recorder during 8 years of monitoring on the Moon [24]. Bigger events with higher return periods can be anticipated as well. For material minimisation purposes the selected embrace angle would be $\beta = 180^\circ$.

Initially, by considering an arch without additional vertical loading than its self-weight (or when the total mass contributes to inertial loading), $L = 1$, the dimensionless inertial loading would be, $\frac{\epsilon}{\alpha L} = 1.2$. Using Fig. 23, the minimum required thickness for a parabolic and circular arch with $\beta = 180^\circ$ will be $\frac{t^p}{R} = 0.58$ and $\frac{t^c}{R} = 0.64$ respectively. This translates to $t^p = 8.70 \text{ m}$ and $t^c = 9.60 \text{ m}$; these extreme values for solid arch thicknesses highlight how important and dominant role the low gravity plays on the stability of arches.

However, after adding a layer of loose regolith shielding that partially participates in the inertial loading with its mass resulting in $L = 3$, the new dimensionless inertial load applied to the arches examined in this example will be $\frac{\epsilon}{\alpha L} = 0.4$. Hence, the minimum required thickness for a parabolic and circular arch with $\beta = 180^\circ$ will be $\frac{t^p}{R} = 0.192$ and

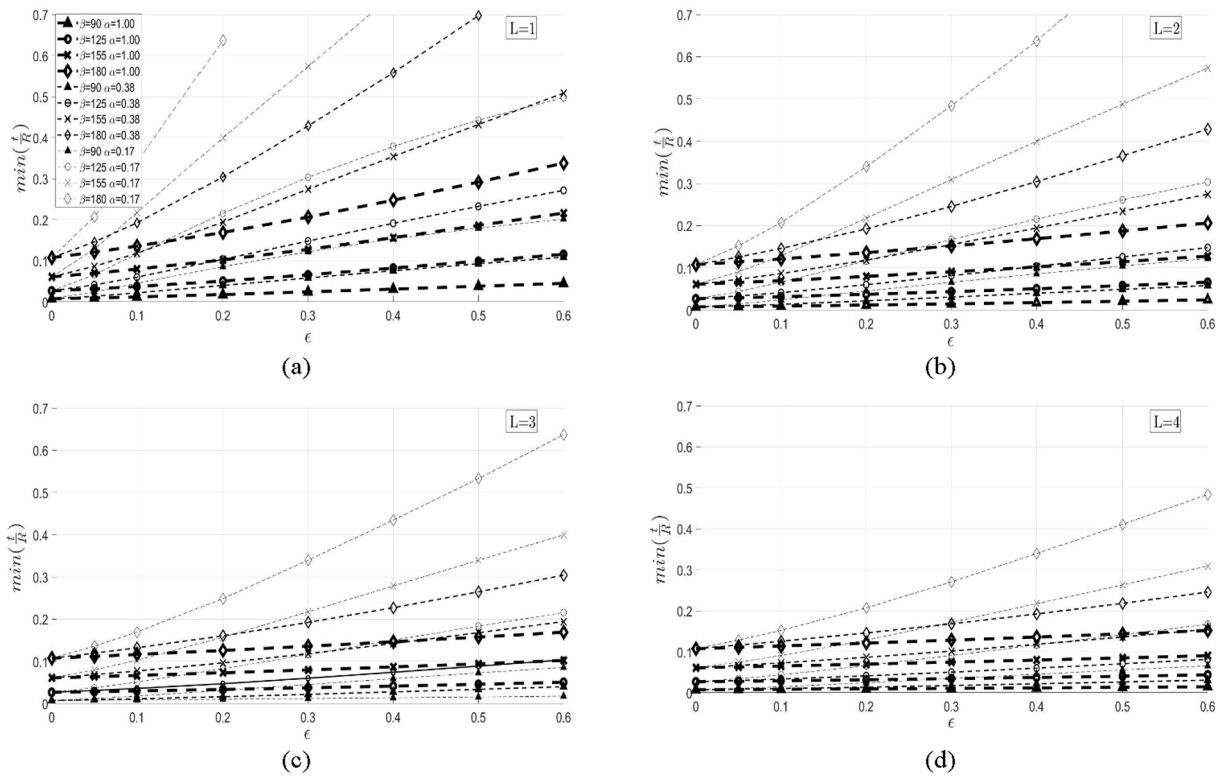


Fig. 20. Minimum t/R versus inertial acceleration for circular arches with various embrace angles $\{\beta = 90^\circ, 125^\circ, 155^\circ \text{ and } 180^\circ\}$, considering low gravity, $\alpha = 1, 0.38, 0.17$, and $L = 1, 2, 3, 4$.

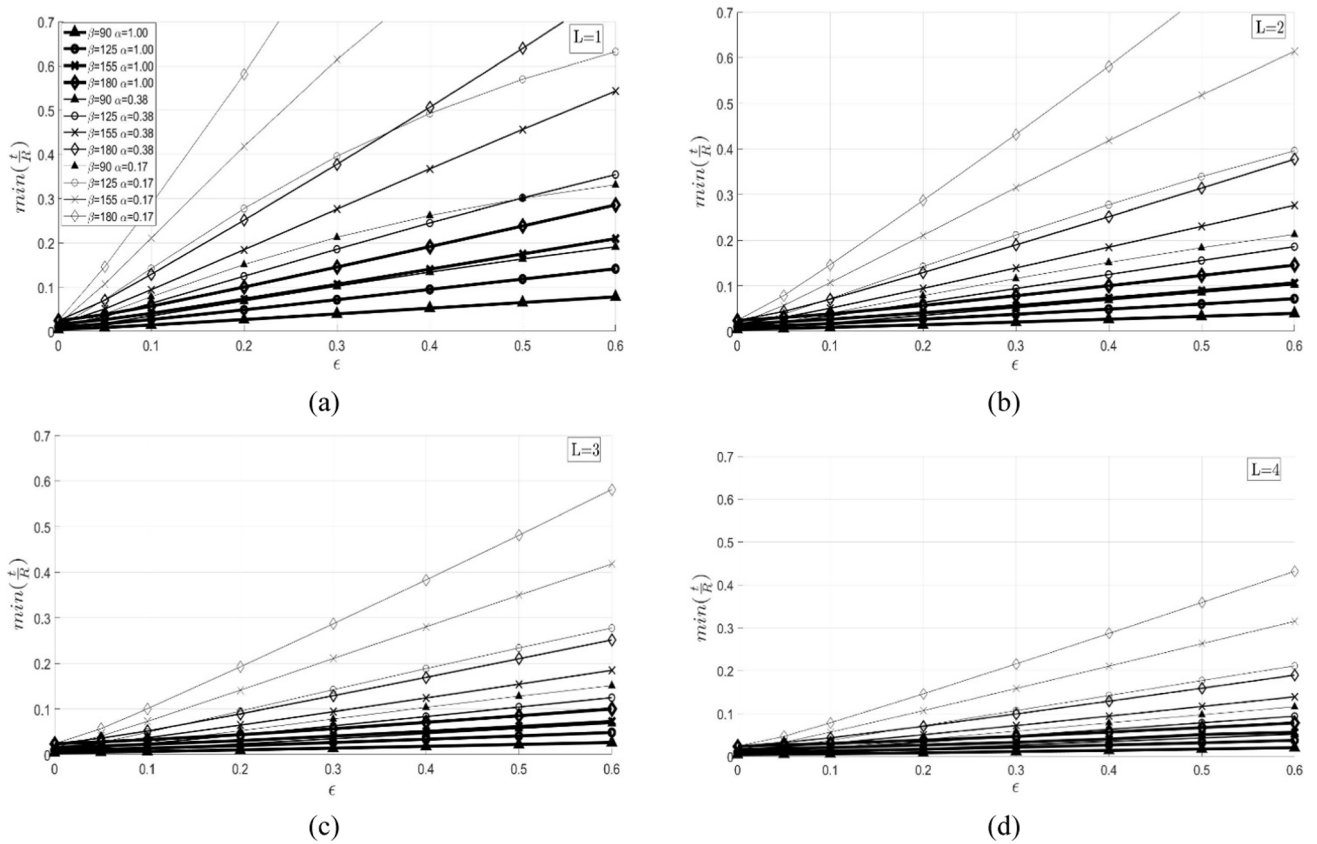


Fig. 21. Minimum t/R versus inertial acceleration for parabolic arches with various embrace angles $\{\beta = 90^\circ, 125^\circ, 155^\circ \text{ and } 180^\circ\}$, considering low gravity, $\alpha = 1, 0.38, 0.17$, and $L = 1, 2, 3, 4$.

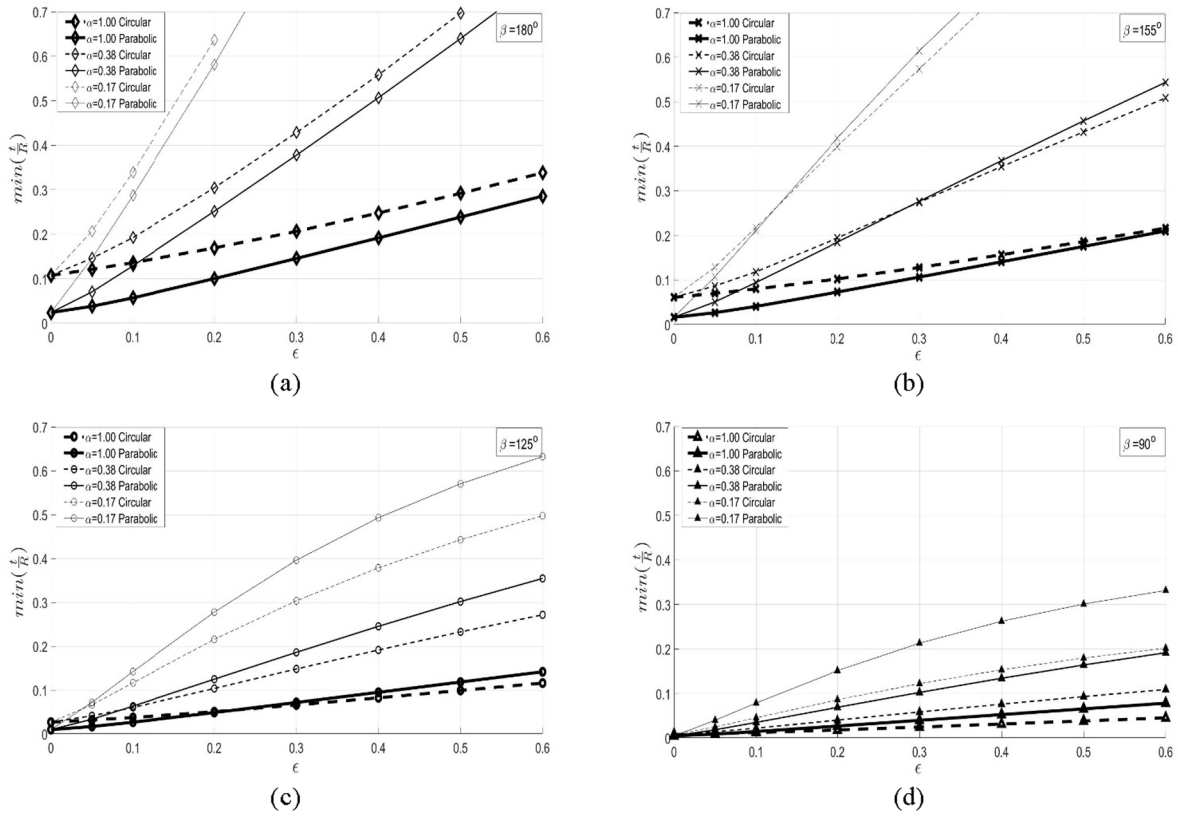


Fig. 22. Minimum t/R versus inertial acceleration for parabolic and circular arches with embrace angles: (a) $\beta = 180^\circ$, (b) $\beta = 155^\circ$, (c) $\beta = 125^\circ$, and (d) $\beta = 90^\circ$ considering low gravity, $\alpha = 1, 0.38, 0.17$ assuming $L = 1$.

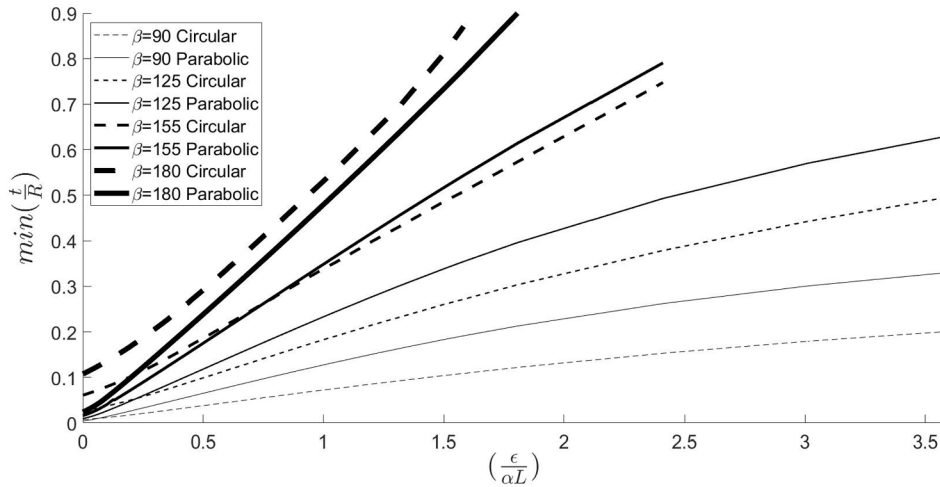


Fig. 23. Master curves of the minimum required t/R versus the dimensionless inertial loading, $\epsilon/(\alpha L)$, for both circular and parabolic arches.

$\frac{\epsilon}{R} = 0.249$ respectively that yields thicknesses of $t^P = 2.88$ m and $t^C = 3.74$ m. Given the above, it is evident that the additional shielding material if placed properly in order not to participate to inertial loading, can lead to less structural material use, regardless of the arch geometry. Another observation is that the minimum shielding thickness, $t_{radiation} = 2.5$ m [6], will be easily satisfied in the case of long-span arches on the Moon.

For comparison reasons, if these arches were to be constructed on Earth for the same given design acceleration and with $L = 1$, they would result in $\frac{\epsilon}{\alpha L} = 0.2$ and thus to $\frac{\epsilon^P}{R} = 0.10$ and $\frac{\epsilon^C}{R} = 0.17$ which yields $t^P = 1.50$ m and $t^C = 2.55$ m. The difference between the results is

impressive and the need to optimise the structural form of extraterrestrial structures becomes even more apparent.

In every case, further finite-element analysis needs to be undertaken to determine the appropriate stress levels before proceeding with the design of any of these arches in order to consider shear forces as well.

6. Conclusions

This paper has investigated the limit-state analysis of circular and parabolic arches when they are subjected to self-, additional vertical weight and inertial loading in low-gravity conditions. The study employs a variational formulation in order to determine the minimum

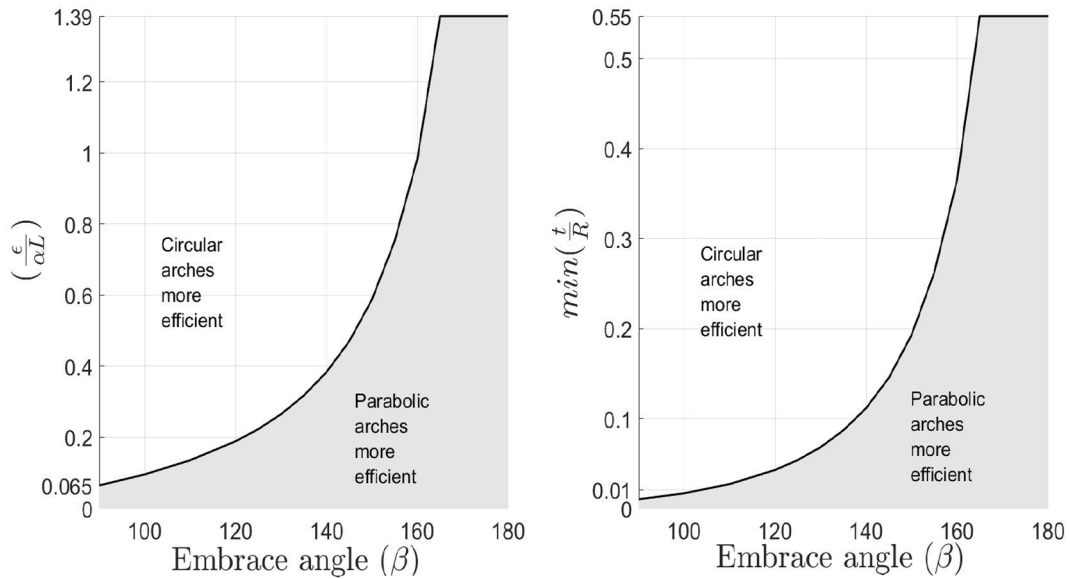


Fig. 24. Identified areas where either the circular or the parabolic arch leads to (i) left: more cost-effective geometries (smaller values of t/R) and (ii) right: more resilient structures that can sustain higher levels of dimensionless inertial loading $\epsilon/(\alpha L)$.

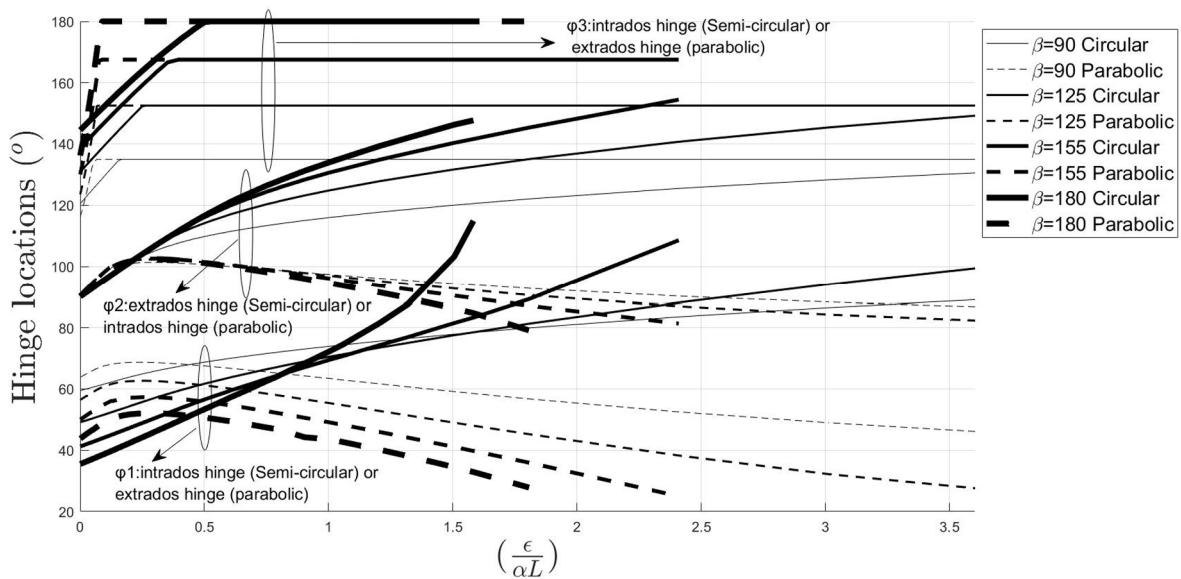


Fig. 25. Master curves of the hinge location versus the dimensionless inertial loading, $\epsilon/(\alpha L)$, for both circular and parabolic arches.

required thickness of the different arches in order not to become a mechanism under the different combinations of loading and gravitational fields.

The results show that parabolic arches require much lower minimum thickness to sustain their own weight compared to circular arches and that they exhibit the symmetrically opposite five-hinge mechanism. This manifests the “geometrical favouritism” towards structures that resemble the catenary shape (parabolic) under self-weight, even though the catenary is not an admissible thrust line [27].

Furthermore, except the fact that larger inertial loading results in higher minimum thickness, smaller embrace angles lead to thinner arches. The latter is evident as when the embrace angle decreases, for a given c , the arc of the arch becomes smaller (the arc corresponds to smaller embrace angle) and therefore requires less structural material. The asymmetrical four-hinge mechanism developed due to the horizontal loading is opposite for the two types of arches. However, the mechanism pattern shows a significant similarity, in the sense that as the

inertial loading increases, in all cases, the mechanism tends to move “upstream” against the horizontal load in order for the arches to accommodate their limit thrust lines. Another interesting observation is that although for an embrace angle $\beta = 180^\circ$ the parabolic is always more beneficial than the semi-circular arch, this is not the case when the embrace angle decreases. For smaller embrace angles and higher inertial loading, the circular shape tends to become more beneficial than the parabolic; a result that was not initially anticipated due to the catenary resemblance of the parabolic shape.

Low-gravity conditions increase the structural material requirements (minimum thickness) significantly, although the additional weight from the loose shielding material can act beneficially, as expected, since gravity provides extra stability to arches. Hence, the need for optimising the structural form of resilient “extraterrestrial” structures becomes more evident. Moreover, a self-similar behaviour has been observed, revealing that every arch of a certain geometry type and embrace angle (β) that is subjected to a “universal” dimensionless inertial load $\frac{\epsilon}{\alpha L}$,

always results in the same minimum thickness and rupture angles $\left\{\frac{t}{R}, \varphi_1, \varphi_2, \varphi_3\right\}$. Areas where the circular or parabolic arches can be more beneficial in terms of structural material are identified and presented in Fig. 22 expressed in terms of the “universal” dimensionless inertial loading and the different embrace angles; these can be used practically for taking important decisions at the preliminary design stage. The need to optimise the arch geometry becomes apparent in low-gravity conditions, as shown in Section 5, since the required minimum thickness can become prohibitively large.

Declaration of Competing Interest

The authors declare that they have no known competing financial

interests or personal relationships that could have appeared to influence the work reported in this paper.

Acknowledgments

This paper is part of the project entitled “*Designing for the Future: Optimising the structural form of regolith-based monolithic vaults in low-gravity conditions*” supported by the Engineering and Physical Sciences Research Council (EPSRC), UK (Scheme: New Investigator Award), led by the University of Greenwich. EPSRC Grant Number: EP/S036393/1.

Appendix A

The coordinates of the extrados and intrados of the parabolic arch are:

$$y_{ex} = \left(R + \frac{t}{2}\right) - \frac{\left(R + \frac{t}{2}\right)}{\left(\frac{R}{2c} + \frac{t}{2}\right)} x^2 \quad (A1)$$

$$y_{in} = \left(R - \frac{t}{2}\right) - \frac{\left(R - \frac{t}{2}\right)}{\left(\frac{R}{2c} - \frac{t}{2}\right)} x^2 \quad (A2)$$

Subsequently, the weight of an arbitrary segment of the arch assuming radial cuts (Fig. 5b) will be:

$$W = \left\{ \int_0^{x_{ex(i)}} (y_{ex} - y_{\rho(i)}) dx - \int_0^{x_{in(i)}} (y_{in} - y_{\rho(i)}) dx \right\} - \left\{ \int_0^{x_{ex(i+1)}} (y_{ex} - y_{\rho(i+1)}) dx - \int_0^{x_{in(i+1)}} (y_{in} - y_{\rho(i+1)}) dx \right\} \quad (A3)$$

where

$$y_{\rho(i)} = x \tan(\varphi_i) \quad (A4a)$$

$$y_{\rho(i+1)} = x \tan(\varphi_{i+1}) \quad (A4b)$$

$$x_{ex(i)} = \left(r_i + \frac{t}{2}\right) \cos(\varphi_i) \quad (A4c)$$

$$x_{ex(i+1)} = \left(r_{i+1} + \frac{t}{2}\right) \cos(\varphi_{i+1}) \quad (A4d)$$

$$x_{in(i)} = \left(r_i - \frac{t}{2}\right) \cos(\varphi_i) \quad (A4e)$$

$$x_{in(i+1)} = \left(r_{i+1} - \frac{t}{2}\right) \cos(\varphi_{i+1}) \quad (A4f)$$

By substituting Eq. (9) into (8) after the consideration of $c = 1/2$, the exact expression of the weight of an arbitrary segment is:

$$W = \left\{ \left(R + \frac{t}{2}\right) x_{ex(i)} - \frac{1}{3 \left(R + \frac{t}{2}\right)} x_{ex(i)}^3 \right\} - \left\{ \frac{1}{2} \tan(\varphi_i) x_{ex(i)}^2 \right\} - \left\{ \left(R - \frac{t}{2}\right) x_{in(i)} - \frac{1}{3 \left(R - \frac{t}{2}\right)} x_{in(i)}^3 \right\} + \left\{ \frac{1}{2} \tan(\varphi_i) x_{in(i)}^2 \right\} - \left\{ \left(R + \frac{t}{2}\right) x_{ex(i+1)} - \frac{1}{3 \left(R + \frac{t}{2}\right)} x_{ex(i+1)}^3 \right\} + \left\{ \frac{1}{2} \tan(\varphi_{i+1}) x_{ex(i+1)}^2 \right\} + \left\{ \left(R - \frac{t}{2}\right) x_{in(i+1)} - \frac{1}{3 \left(R - \frac{t}{2}\right)} x_{in(i+1)}^3 \right\} - \left\{ \frac{1}{2} \tan(\varphi_{i+1}) x_{in(i+1)}^2 \right\} \quad (A5)$$

The equations for the calculation of the coordinates of the centre of gravity of an arbitrary segment of the arch are presented below.

$$x_c = \frac{\left\{ \int_0^{x_{ex(i)}} (y_{ex} - y_{\rho(i)}) x dx - \int_0^{x_{in(i)}} (y_{in} - y_{\rho(i)}) x dx \right\} - \left\{ \int_0^{x_{ex(i+1)}} (y_{ex} - y_{\rho(i+1)}) x dx - \int_0^{x_{in(i+1)}} (y_{in} - y_{\rho(i+1)}) x dx \right\}}{W} \quad (A6a)$$

$$y_c = \frac{\left\{ \int_0^{x_{ex(i)}} \left(\frac{y_{ex}^2}{2} - \frac{y_{\rho(i)}^2}{2}\right) dx - \int_0^{x_{in(i)}} \left(\frac{y_{in}^2}{2} - \frac{y_{\rho(i)}^2}{2}\right) dx \right\} - \left\{ \int_0^{x_{ex(i+1)}} \left(\frac{y_{ex}^2}{2} - \frac{y_{\rho(i+1)}^2}{2}\right) dx - \int_0^{x_{in(i+1)}} \left(\frac{y_{in}^2}{2} - \frac{y_{\rho(i+1)}^2}{2}\right) dx \right\}}{W} \quad (A6b)$$

$$x_c = \left\{ \left(\frac{1}{2} \left(R + \frac{t}{2} \right) x_{ex(i)}^2 - \frac{1}{4 \left(R + \frac{t}{2} \right)} x_{ex(i)}^4 \right) - \left(\frac{1}{3} \tan(\varphi_i) x_{ex(i)}^3 \right) - \left(\frac{1}{2} \left(R - \frac{t}{2} \right) x_{in(i)}^2 - \frac{1}{4 \left(R - \frac{t}{2} \right)} x_{in(i)}^4 \right) + \left(\frac{1}{3} \tan(\varphi_i) x_{in(i)}^3 \right) - \left(\frac{1}{2} \left(R + \frac{t}{2} \right) x_{ex(i+1)}^2 - \frac{1}{4 \left(R + \frac{t}{2} \right)} x_{ex(i+1)}^4 \right) + \left(\frac{1}{3} \tan(\varphi_{i+1}) x_{ex(i+1)}^3 \right) + \left(\frac{1}{2} \left(R - \frac{t}{2} \right) x_{in(i+1)}^2 - \frac{1}{4 \left(R - \frac{t}{2} \right)} x_{in(i+1)}^4 \right) - \left(\frac{1}{3} \tan(\varphi_{i+1}) x_{in(i+1)}^3 \right) \right\} / W$$

$$y_c = \left\{ \left(\frac{1}{10 \left(R + \frac{t}{2} \right)^2} x_{ex(i)}^5 - \frac{1}{3} x_{ex(i)}^3 + \frac{1}{2} \left(R + \frac{t}{2} \right)^2 x_{ex(i)} \right) - \left(\frac{1}{6} \tan^2(\varphi_i) x_{ex(i)}^3 \right) - \left(\frac{1}{10 \left(R - \frac{t}{2} \right)^2} x_{in(i)}^5 - \frac{1}{3} x_{in(i)}^3 + \frac{1}{2} \left(R - \frac{t}{2} \right)^2 x_{in(i)} \right) + \left(\frac{1}{6} \tan^2(\varphi_i) x_{in(i)}^3 \right) - \left(\frac{1}{10 \left(R + \frac{t}{2} \right)^2} x_{ex(i+1)}^5 - \frac{1}{3} x_{ex(i+1)}^3 + \frac{1}{2} \left(R + \frac{t}{2} \right)^2 x_{ex(i+1)} \right) + \left(\frac{1}{6} \tan^2(\varphi_{i+1}) x_{ex(i+1)}^3 \right) + \left(\frac{1}{10 \left(R - \frac{t}{2} \right)^2} x_{in(i+1)}^5 - \frac{1}{3} x_{in(i+1)}^3 + \frac{1}{2} \left(R - \frac{t}{2} \right)^2 x_{in(i+1)} \right) - \left(\frac{1}{6} \tan^2(\varphi_{i+1}) x_{in(i+1)}^3 \right) \right\} / W$$

Appendix B. Supplementary material

Supplementary data to this article can be found online at <https://doi.org/10.1016/j.engstruct.2020.111501>.

References

- Alexakis H, Makris N. Minimum thickness of elliptical masonry arches. *Acta Mech* 2013;224(12):2977–91.
- Alexakis H, Makris N. Structural stability and bearing capacity analysis of the tunnel-entrance to the stadium of ancient Nemea. *Int J Architect Herit* 2013;7(6): 673–92.
- Alexakis H, Makris N. Limit equilibrium analysis and the minimum thickness of circular masonry arches to withstand lateral inertial loading. *Arch Appl Mech* 2014;84(5):757–72.
- Deeks Andrew J, Hao Hong. Developments in mechanics of structures & materials. In: Proceedings of the 18th Australasian conference on the mechanics of structures and materials, Perth, Australia, 1–3 December 2004; 2004.
- Aulesa V, Ruiz F, Casanova I. Structural requirements for the construction of shelters on planetary surfaces. *Space* 2000; 2000.
- Benaroya H, Bernold L, Chua KM. Engineering, design and construction of lunar bases. *J Aerosp Eng* 2002;15(2):33–45.
- Block P, DeJong M, Ochsendorf J. As hangs the flexible line: equilibrium of masonry arches. *Nexus Netw J* 2006;8(2):13–24.
- Chow BJ, Chen T, Zhong Y, Qiao Y. Direct formation of structural components using a Martian soil simulant. *Sci Rep* 2017;7:1–8.
- Clemente P. Introduction to dynamics of stone arches. *Earthq Eng Struct Dyn* 1998; 27:513–22.
- Coulomb CA. Essai sur une application des règles des maximis et minimis à quelques problèmes de statique relatifs à l'architecture. Mémoires de mathématique et de physique, présentés à l'académie royal des sciences per divers savants et lus dans ses assemblées, Paris (1776) 1773; 7: 343–82.
- Couplet P. De la poussée des voûtes. Histoire de l'Académie Royale des Sciences, Paris (1731, 1732), pp. 79–117 and pp. 117–141 (1729, 1730).
- De Kestelier X, Dini E, Cesaretti G, Colla V, Pambaguian L. Lunar outpost design. Research and development; 2015. Available online at https://www.fosterandpartners.com/media/2634652/Lunar_outpost_design_foster_and_partners.pdf.
- Dorman J, Evans S, Nakamura Y, Latham G. On the timevarying properties of the Lunar seismic meteoroid population. In: Proc. lunar planet. sci. conf. 9th; 1978. p. 3615–26.
- Duennebier F, Dorman J, Lammlein D, Latham G, Nakamura Y. Meteoroid flux from passive seismic experiment data. In: Proc. lunar sci. conf. 6th; 1975. p. 2417–26.
- El-Derby AOD, Elyamani A. The adobe barrel vaulted structures in ancient Egypt: a study of two case studies for conservation purposes. *Mediterranean Archaeol Archaeometry* 2016;16(1):295–315.
- Gáspár O, Sipos AA, Sajtos I. Effect of stereotomy on the lower bound value of minimum thickness of semi-circular masonry arches. *Int J Architect Herit* 2018;12(6):899–921.
- Gohnert M, Bradley R. Catenary solutions for arches and vaults. *J Archit Eng* 2020; 26(2):04020006.
- Goulas A, Binner JGP, Harris RA, Friel RJ. Assessing extraterrestrial regolith material simulants for in-situ resource utilisation based 3D printing. *Appl Mater Today* 2017;6:54–61.
- Gregory D. Catenaria. *Philos Trans* 1698;19:637–52.
- Hooke R. A description of helioscopes, and some other instruments. London; 1675.
- Iserles A. A first course in the numerical analysis of differential equations. Cambridge University Press; 2008.
- Heyman J. Equilibrium of shell structures. Oxford University Press; 1977. p. 1–134.
- Jablonski AM, Ogden KA. Technical requirements for lunar structures. *J Aerosp Eng* 2008;21(2):72–90.
- Kalopodis N, Kampas G, Ktenidou O-J. A review towards the design of extraterrestrial structures: from regolith to human outposts. *Acta Astronaut* 2020; 175:540–69.
- Kalopodis N, Kampas G, Ktenidou O-J. Revisiting the fundamental structural dynamic systems: the effect of low gravity. *Arch Arch Appl Mech* 2019;10: 1861–84.
- Kalopodis N, Kampas G, Webb J, Ktenidou O-J. The effect of self-weight on free-standing blocks. In: 2nd International Conference on Natural Hazards & Infrastructures (ICONHIC 2019); 2019.
- Makris N, Alexakis H. The effect of stereotomy on the shape of the thrust-line and the minimum thickness of semicircular masonry arches. *Arch Appl Mech* 2013;83(10):1511–33.
- Michiels T, Napolitano R, Adriaenssens S, Glisic B. Comparison of thrust line analysis, limit state analysis and distinct element modeling to predict the collapse load and collapse mechanism of a rammed earth arch. *Eng Struct* 2017;148: 145–56.
- Michiels T, Adriaenssens S. Form-finding algorithm for masonry arches subjected to in-plane earthquake loading. *Comput Struct* 2018;195:85–98.
- Milankovitch, M. Beitrag zur Theorie der Druckkurven. Dissertation zur Erlangung der Doktorwürde, K.K. technische Hochschule, Vienna; 1904.
- Nakamura Y, Latham GV, Dorman HJ. How we processed Apollo Lunar seismic data. *Phys Earth Planet Inter* 1980;21(2–3):218–24.
- Nikolić D. Thrust line analysis and the minimum thickness of pointed masonry arches. *Acta Mech* 2017;228(6):2219–36.
- Nikolić D. Catenary arch of finite thickness as the optimal arch shape. *Struct Multidiscip Optim* 2019;60(5):1957–66.
- Oberst J, Nakamura Y. A seismic risk for the Lunar base. In: The second conf. on lunar bases and space activities of the 21st century. Vol. 1, NASA, Washington, DC; 1992. p. 231–3.
- Ochsendorf J. Collapse of masonry structures. PhD Dissertation. Cambridge: Department of Engineering, University of Cambridge; 2002.
- Poleni G. Memorie storiche della gran cupola del tempio Vaticano e de' danni di essa, e de' ristoramenti loro. Stamperia del Seminario, Padova; 1748.
- Rapp D. Use of extraterrestrial resources for human space missions to moon or mars; 2018.
- Reitz G, Berger T, Matthiae D. Radiation exposure in the moon environment. *Planet Space Sci* 2012;74(1):78–83.
- Ricci E, Fraddosio A, Piccioni MD, Sacco E. A new numerical approach for determining optimal thrust curves of masonry arches. *Eur J Mech A Solids* 2019.
- Rodrigues JD. Defining, mapping and assessing deterioration patterns in stone conservation projects. *J Cult Herit* 2015;16(3):267–75.
- Sacco E. Some aspects on the statics of masonry arches. In: *Masonry structures: between mechanics and architecture*. Cham: Springer International Publishing; 2015. p. 265–90.

- [42] [Tempesta G, Galassi S. Safety evaluation of masonry arches. A numerical procedure based on the thrust line closest to the geometrical axis. Int J Mech Sci 2019;155: 206–21.](#)
- [43] [Trial M. Some effects of declining US university civil engineering enrollments on the space enterprise. Space 2000; 2000.](#)
- [44] [Wilkinson S, Musil J, Dierckx J, Gallou I, De Kestelier X. Autonomous Additive Construction on Mars. In: Earth and space 2016: engineering for extreme environments – proceedings of the 15th biennial international conference on engineering, science, construction, and operations in challenging environments; 2016. p. 343–53.](#)
- [45] [Wolfram PJ, Lorenz WF. Longstanding design: roman engineering of aqueduct arcades. Int J History Eng Technol 2016;86\(1\):56–69.](#)